Journal of Geodesy (2026) 100:7
https://doi.org/10.1007/s00190-025-02028-3

ORIGINAL ARTICLE

Estimation of regional ice mass trends in Greenland using a global inversion of level-2 satellite gravimetry data

Pavel Ditmar[1]

Received: 16 August 2024 / Accepted: 23 December 2025

Abstract

A methodology has been developed for an accurate estimation of mass anomalies in the Earth system using level-2 data products from satellite gravimetry GRACE and GRACE Follow-On (GFO) missions. Its key elements are: (i) direct inversion of Spherical Harmonic Coefficients (SHCs)—or SHC trends—into a global distribution of mass anomalies (or their trends); (ii) Spatially-varying regularization that takes into account available information about the behavior of mass anomalies; and (iii) rigorous optimization of the data processing consistently with the target estimates. The methodology is applied to quantify the mass balance of the Greenland Ice Sheet and its individual Drainage Systems (DSs) in Apr. 2002–Aug. 2023 on the basis of GRACE/GFO monthly solutions from the Institute of Geodesy at Graz University of Technology (ITSG). It is found that the rate of the total mass loss in Greenland was 271 ± 10 Gt/yr. It varied between 19 ± 4 Gt/yr in northeast DS and 77 ± 7 Gt/yr in southeast DS. In average, the mass balance of individual DSs is estimated with an accuracy better than 5 Gt/yr. As a consequence, the obtained estimates show a sufficiently high signal-to-noise ratio (between 5 in the northeast DS and 42 in the northwest DS). This opens the door, among other, for using GRACE/GFO data for a comparison, validation, and calibration of physical models describing mass changes in Greenland, including its surface mass balance, at the scale of individual DSs.

Keywords GRACE · GFO · Spherical harmonic coefficients · Stokes coefficients · Tikhonov regularization · Ice mass balance

1 Introduction

In the course of the last two decades, satellite gravimetry became one of the most important tools to study mass transport in the Earth system. The two primary satellite missions that delivered and still deliver data for that purpose are Gravity Recovery and Climate Experiment (GRACE) launched in 2002 (Tapley et al. 2004) and its successor GRACE Follow-On (GFO) launched in 2018 (Landerer et al. 2020). As a next step, Mass-change And Geosciences International Constellation (MAGIC) will be launched in phases within the next few years (Daras et al. 2024).

The data collected by GRACE and GFO missions have been successfully applied, among other, in hydrology (Güntner 2008; Frappart and Ramillien 2018; Rodell et al. 2018), studies of ice sheets and mountain glaciers (Luthcke et al. 2006; Forsberg et al. 2017; Cirací et al. 2020; Velicogna et al. 2020), climatology (Cazenave et al. 2009; Meyssignac et al. 2019; Tapley et al. 2019), oceanography (Han et al. 2005; Peralta-Ferriz et al. 2014; Landerer et al. 2015), estimation of geocenter variations (Swenson et al. 2008; Sun et al. 2017), and solid Earth studies (Han et al. 2006; Paulson et al. 2007; Wang and Burgmann 2019).

Until recently, GRACE data were predominantly shared with the scientific community in the form of level-2 data product (Bettadpur 2018; Dahle et al. 2018; Yuan 2018). This data product contains time-series of monthly estimates of the Earth's gravitational field, where every solution is provided as a set of Spherical Harmonic Coefficients (SHCs) complete to a given maximum degree, in most cases 60 or 96 (Heiskanen and Moritz 1984). On this basis, SHC variations can be computed as the difference between the current (e.g., monthly) SHC values and their long-term means. Then, conversion of SHC variations into mass anomalies can be easily done with the spherical harmonic synthesis (Wahr et al. 1998; Ditmar 2018). Unfortunately, SHCs provided by satellite gravimetry are contaminated with noise, which rapidly increases with spherical harmonic degree and manifests itself in the spatial domain as north-south stripes. Therefore, mass

✉ Pavel Ditmar
p.g.ditmar@tudelft.nl

[1] Delft University of Technology, Stevinweg 1, 2628 CN Delft, The Netherlands

Published online: 23 January 2026

anomalies obtained by means of the straightforward spherical harmonic synthesis may be rather inaccurate, even if the maximum spherical harmonic degree is only 60. To cope with that problem, a large number of various low-pass filters have been developed (e.g., Wahr et al. 1998; Swenson and Wahr 2006; Kusche 2007; Klees et al. 2008; Siemes et al. 2013, etc). However, any filter suppresses in practice not only noise, but also signal. Another drawback of the straightforward spherical harmonic synthesis is its inability to take into account various additional information, such as the fact that mass anomalies over land are typically much larger than over the ocean. Finally, GRACE and GFO missions are unable to provide sufficiently accurate estimates of some low-degree SHCs (namely, degree-1, $C_{2,0}$, and, sometimes, $C_{3,0}$ coefficients). Therefore, the level-2 data delivered by these missions have to be complemented with information from other sources (Cheng et al. 2013; Sun et al. 2016, 2017; Loomis et al. 2020).

An alternative, which is getting more and more popular nowadays, is to exploit level-3 data products—ready-to-use mass anomalies at the Earth surface. Such data are typically provided as mass anomalies at the patches of a pre-defined geometry, the so-called "mascons" (Luthcke et al. 2006, 2013; Loomis et al. 2019; Croteau et al. 2021). Those data products are usually computed by a regularized inversion of raw (level-1b) GRACE/GFO data. Unfortunately, the optimal choice of regularization strongly depends on the exact definition of the mass anomaly estimates of interest. For instance, the optimal estimation of mass anomalies at the monthly scale requires much more aggressive regularization than the optimal estimation of long-term trends (Loomis et al. 2021). We believe, therefore, that ready-to-use mascon-type data product offers in many cases only sub-optimal estimates of mass anomalies.

Whatever approach to an estimation of mass anomalies at the Earth surface is implemented, the resulting estimates are subject to various inaccuracies. Those inaccuracies have a significant impact on all the estimated mass anomalies. This concerns, among other, ice mass losses in Greenland, which is the primary focus of our study. Ice mass loss in Greenland attracts a close attention of both the society and the scientific community due to the fact that the Greenland Ice Sheet (GrIS) has been a major contributor to global sea level rise in recent decades. In average, it added about 0.47 mm to global mean sea level rise every year between 1991 and 2015 (van den Broeke et al. 2016), which corresponds the annual mass loss rate of 170 Gt/yr. Furthermore, it is likely that ice mass losses in Greenland will accelerate in the coming decades (Sellevold and Vizcaino 2020).

The error budget of GRACE/GFO-bases estimates of ice mass losses in Greenland was analyzed, among other, by Velicogna and Wahr (2013), Bonin and Chambers (2013), and Xu et al. (2015). According to Velicogna and Wahr (2013), the following contributors to this error budget can be identified:

- Lacking vertical resolution of satellite gravimetry, which results in the contamination with signals originated below and above the Earth surface (namely, due to Glacial Isostatic Adjustment (GIA) and atmosphere, respectively).
- Coarse horizontal resolution of satellite gravimetry, which results in so-called signal leakage; this can be exacerbated by the post-processing applied (e.g., filtering).
- Limited temporal resolution of GRACE data, which requires an application of various background models to estimate and subtract the impact of rapid mass transport processes (predominantly in the atmosphere and ocean); the uncertainties of those background models also contribute to the noise budget.
- Measurement errors in GRACE data, which are caused by inaccuracies of the onboard sensors (in the first instance, accelerometers and inter-satellite ranging systems).

The uncertainty of ice mass loss rates integrated over entire Greenland estimated from GRACE/GFO data typically stays at the level of about 40 Gt/yr (Velicogna et al. 2020; Loomis et al. 2021), whereas mass loss rates integrated over individual Drainage Systems (DSs) are typically provided without realistically estimated errors margins (if at all). This seems to be sufficient to quantify the *current* contribution of the GrIS to the global sea level rise. However, it is even more important to make accurate projections of this contribution onto the coming years and decades. To that end, the mechanisms behind the observed ice mass changes must be understood in detail. This implies a need in accurate geophysical models of all those mechanisms, which requires a sufficiently high accuracy of mass change estimates for validation and calibration purposes. For instance, the relative uncertainty of the Regional Atmospheric Climate Model RACMO (Noël et al. 2016) describing the Surface Mass Balance (SMB) in Greenland is of the order of 10% (more specifically, 9% and 15% in the context of precipitation and runoff modelling, respectively; van den Broeke et al. 2016; Ran et al. 2018b). This means that an assessment or/and improvement of that model requires at least an order of magnitude higher Signal-to-Noise Ratio than that sufficient in the context of the total signal quantification. Thus, a production of independent highly accurate estimates of ice mass losses in Greenland remains an utterly relevant task. Importantly, the performance of geophysical models to be validated may be different in different parts of Greenland. Therefore, independent accurate estimates of ice mass losses must address not only the GrIS as a whole, but also its individual Drainage Systems (DSs) separately.

The major goal of this study is to demonstrate how the accuracy of GRACE/GFO-based mass anomaly estimates

can be radically improved, using the long-term mass balance of the GrIS as a test case. Mass change rates integrated over both entire Greenland and individual DSs are considered. We would like to stress that the presented methodology can be easily adapted to other cases than that considered in this publication (i.e., to different regions, time scales, and signals of interest).

To reach our goal, we compute our own global solution of a mascon type, using the level-2 data products (namely, SHCs) as input. A somewhat similar approach was considered, e.g., in Croteau et al. (2021) and Chang et al. (2023). To optimize the obtained estimates, a tailored regularization scheme is developed. Such an approach offers a number of important benefits:

- In contrast to the approaches exploiting spherical harmonic synthesis, it is not necessary to truncate the spherical harmonic expansion and/or implement a low-pass filter to ensure a suppression of high-frequency noise. In our case, such a suppression is a natural outcome of using a regularization that takes into account the stochastic model of errors in SHCs. Such a model can be formed from the provided information about the Standard Deviations (StDs) of errors in SHCs or (if available) from the full variance-covariance matrices of those errors.
- Available additional information about mass anomalies (e.g., geometry of coast lines) can be easily taken into account by an appropriate definition of the regularization scheme.
- Statistically-optimal combination of GRACE/GFO data with other measurements (e.g., those from satellite altimetry) can be easily implemented.
- It is not necessary to incorporate additional information about low-degree SHCs that are not provided by satellite gravimetry; only available SHCs can be used as input.
- Usage of a *global* inversion, in spite of the focus on a single region (Greenland), allows one to account for mass anomalies outside the target region, so that it is not necessary to use additional background models to mitigate the signal leakage from outside the target region.
- Computation of one's own solution, instead of using an off-the-shelf data product, allows the inversion scheme to be optimized for the estimates of interest, taking into account their definition both in the spatial domain (in our case, mass anomalies integrated over Greenland and over individual DSs) and in the time domain (in our case, the rates of long-term mass changes, i.e., linear trends, in the time intervals of choice).

With this study, we demonstrate that this approach allows the accuracy of the target estimates to be dramatically improved, as compared to the estimates produced so far.

The structure of this paper is as follows. In Sect. 2, we provide general information about the study set-up (model parameterization, primary input data). In Sect. 3, we present in detail the data processing scheme applied to a time-series of GRACE/GFO monthly solutions. In Sect. 4, we present a numerical study aimed at the optimization of the regularization scheme—the key element of the accurate data processing. In Sect. 5, we quantify the errors in the estimated parameters when the selected data processing scheme is applied. In Sect. 6, we focus on an estimation of mass trends in Greenland from real GRACE/GFO data and a comparison of the results with those published earlier. Sect. 7 is devoted to a further discussion of mass anomaly estimation using the global inversion of SHCs. Conclusions of our study are formulated in Sect. 8.

2 Estimation of the long-term mass balance of the GrIS: general information

2.1 Parameterization

Our goal is to estimate the regional mass trends, i.e., the long-term ice mass balance, both per Greenland DS and for all of Greenland, in the 21-year time interval (Apr. 2002–Aug. 2023). To that end, we estimate mass trends in terms of Equivalent Water Height (EWH) using a global equiangular grid. Despite a limited spatial resolution of GRACE/GFO data, we keep the cell size small: 1° (East-West direction) times 0.4° (North-South direction). Within the territory of Greenland, such cells vary in size between 55×44 km in the south and 14×44 km in the north. This allows prior information about the behavior of EWH anomalies to be accurately incorporated into the inversion procedure. For instance, this concerns the geometry of coast lines.

The EWH trends estimated per cell are integrated over entire Greenland and over individual DSs. The total number of DSs is six; their geometries (after the adopted discretization) can be seen in the left panel in Fig. 1. The geometry of these DSs was provided by the IMBIE-3 project (Otosaka et al. 2023) as "Rignot Basins" (Rignot et al. 2011). It is worth noticing that the original DS geometry is limited to the ice sheet territory. However, the spatial resolution of satellite gravimetry is limited to about 300 km, so that we do not distinguish mass changes within the ice sheet from those in the surrounding areas located between the ice sheet margins and the Greenland coast. In view of that, we have manually extended the provided DSs borders down to the coast line.

2.2 Primary input data

As the primary input, we use the time-series of monthly GRACE/GFO solutions called ITSG-Grace2018, which were produced by the Institute of Geodesy at the Graz University of Technology (Kvas et al. 2019). This is one of the most

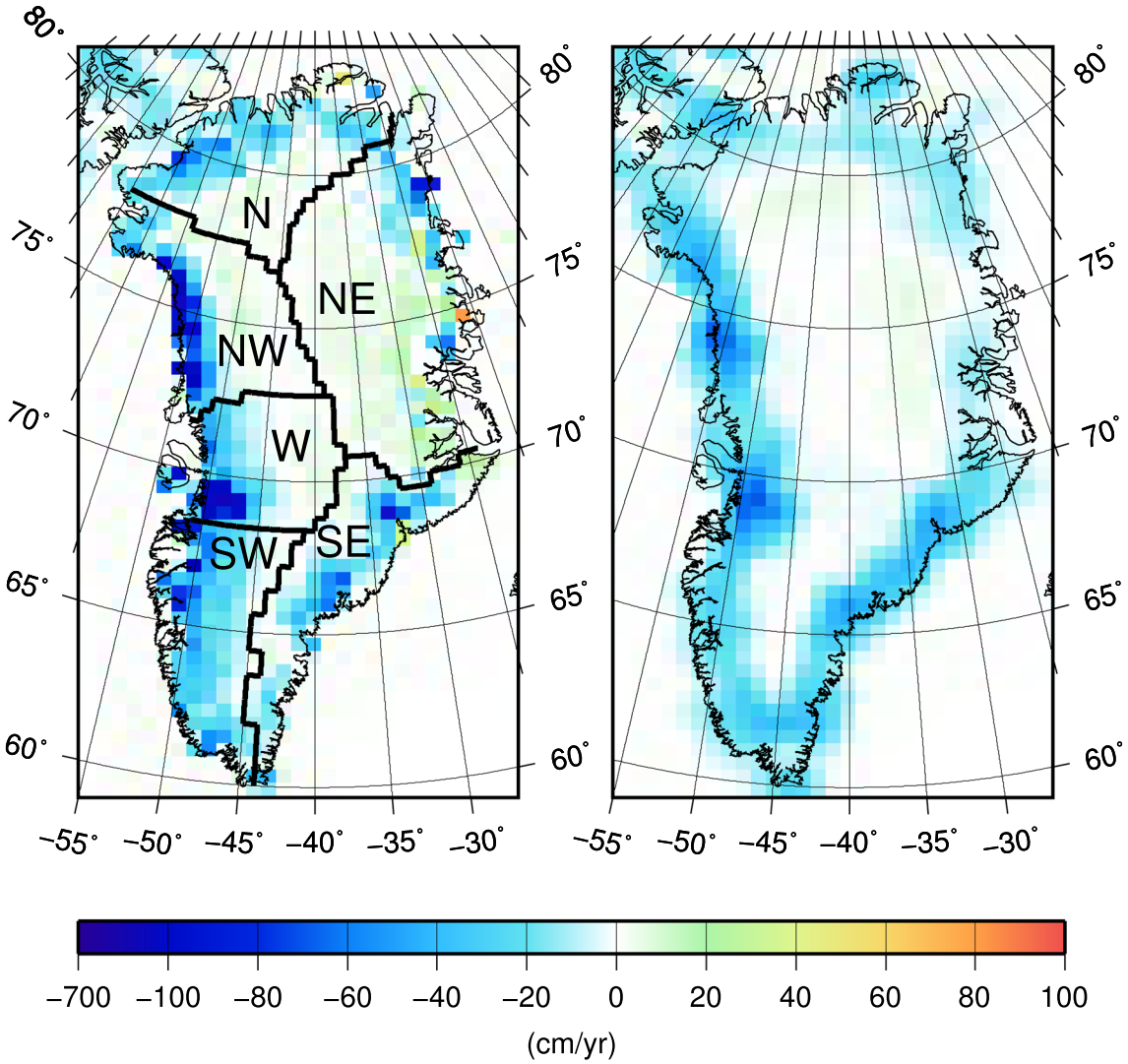

Fig. 1 Adopted geometry of DSs and the "true" EWH trends used in the optimization of the regularization scheme (left panel); EWH trends from the global GSFC mascon solution (Loomis et al. 2021), which describes the mean rates of mass change in Apr. 2002–Sep. 2020 (right panel). The "true" EWH trends within Greenland are based on the elevation trends derived from Cryosat-2 altimetry data collected in 2011–2015 (Simonsen and Sørensen 2017). The "true" EWH trends outside Greenland are taken over from the global GSFC mascon solution

accurate GRACE/GFO level-2 data products at this moment (Ditmar 2022). Each input monthly solution consists of SHCs up to degree 120, each of which is supplied with an error StD. The primary goal of using the ITSG-Grace2018 monthly solutions is to compute the definitive estimates of the ice mass balance in Greenland (Sect. 6.1). Furthermore, the error StDs provided as a part of those solutions are used to define the data weights, which are applied throughout the entire study. We ignore nine monthly solutions in the time interval under consideration to ensure a full consistency between ITSG-Grace2018a solution time-series and alternative ones, which are used below in the quantification of the noise budget (see Sect. 5.4 and 5.5). More specifically, these months are: 07–10.2004, 04.2012, 06–07.2012, and 01–02.2015. In addition, we deliberately ignore the degree-1, $C_{2,0}$, and $C_{3,0}$ SHCs in the provided datasets (unless explicitly stated otherwise). This is to demonstrate that the proposed data processing scheme allows accurate estimates to be obtained even in the absence of low-degree coefficients (in contrast to schemes based on the spherical harmonic synthesis). All the considered SHCs are corrected for the effect of GIA using the ICE-6G model (Stuhne and Peltier 2015).

A large number of additional datasets are used in the course of data processing optimization and quantification of the noise budget below. For the reader's convenience, these datasets are introduced in the further sections as soon as they are needed.

3 Theory

3.1 Derivation of long-term linear trends

We estimate the linear trend per SHC using the weighted least-squares adjustment. Parameters describing an acceleration, an annual, and a semi-annual cycle are co-estimated, so that the corresponding functional model (to be satisfied in the least-squares sense) is defined as follows:

$$\bar{C}_{l,m}^{(0)} + \dot{\bar{C}}_{l,m}\tau_i + \frac{1}{2}\ddot{\bar{C}}_{l,m}\tau_i^2 + \bar{C}_{l,m}^{(sin_1)}\sin\omega\tau_i + \bar{C}_{l,m}^{(cos_1)}\cos\omega\tau_i + \bar{C}_{l,m}^{(sin_2)}\sin 2\omega\tau_i + \bar{C}_{l,m}^{(cos_2)}\cos 2\omega\tau_i = \bar{C}_{l,m}(\tau_i), \quad (1)$$

where $\dot{\bar{C}}_{l,m}$ is the trend (the mean rate of change) to be used in the further analysis; $\bar{C}_{l,m}^{(0)}$, $\ddot{\bar{C}}_{l,m}$, $\bar{C}_{l,m}^{(sin_1)}$, $\bar{C}_{l,m}^{(cos_1)}$, $\bar{C}_{l,m}^{(sin_2)}$, and $\bar{C}_{l,m}^{(cos_2)}$ are co-estimated parameters (which are not used any further); $\bar{C}_{l,m}(\tau_i)$ are the provided SHCs for the i-th month; $\omega = \frac{2\pi}{1\,\mathrm{yr}}$; and τ_i is time relatively to a reference moment t_0:

$$\tau_i = t_i - t_0. \quad (2)$$

This reference moment is defined as the middle of the considered time interval to prevent an absorption of the estimated linear trend by the acceleration $\ddot{\bar{C}}_{l,m}$. Indeed, the corresponding functions of time (τ and $\frac{1}{2}\tau^2$) are orthogonal as soon as the considered interval is symmetric with respect to zero.

We produce the statistically-optimal estimates of the unknown coefficients listed above by applying the weights defined in line with the error StDs that accompany the provided SHCs (unless a different approach is explicitly stated). Furthermore, we quantify the errors in the estimated trends by means of the standard error propagation. Those errors are used to define the weight matrix, which is used in the estimation of EWH trends throughout our study.

3.2 Relationship between SHC trends and mass anomaly trends

A set of SHC trends is directly inverted into EWH trends per cell of a global equiangular grid. We take into account the Earth's oblateness by assuming that mass anomalies are distributed over the surface of the reference ellipsoid, so that the accuracy of the resulting estimates is improved. This is particularly relevant for polar areas, small spatial scales, and long time scales (Ditmar 2018). The explicit relationship between SHC trends and mass anomaly trends directly follows from Eq. (A.5) given in Appendix A. Though that equation was derived for SHCs variations and mass anomalies themselves, it is equally applicable to the corresponding linear trends.

In practice, we use a discrete analog of Eq. (A.5), so that the unknown EWH trends are parameterized with a finite number of values (one value per cell of a global equiangular grid). In view of this, the functional model exploited in the data inversion can be written in the form of a matrix-to-vector multiplication:

$$\mathbf{A}\mathbf{h} = \mathbf{d} \quad (3)$$

where $\mathbf{d}$ is the data vector composed of SHC trends; $\mathbf{h}$ is the vector composed of unknown EWH linear trend per cell; and $\mathbf{A}$ is the design matrix that describes the relationship between the two vectors in line with Eq. (A.5). The explicit expression for the integration of a function over a rectangular cell at the surface of an ellipsoid of rotation is derived in Appendix B.

3.3 Data inversion and stochastic model of data noise

The vector of unknown parameters is computed by a regularized inversion of the data:

$$\mathbf{h} = \left(\mathbf{A}^T {\mathbf{C_d}}^{-1}\mathbf{A} + \mathbf{R}\right)^{-1}\mathbf{A}^T {\mathbf{C_d}}^{-1}\mathbf{d}, \quad (4)$$

where $\mathbf{R}$ is a regularization matrix (see the next section) and $\mathbf{C_d}$ is the error variance-covariance matrix of vector $\mathbf{d}$. In our study, this matrix is defined as a diagonal matrix with elements determined in the course of the error propagation explained in Sect. 3.1. An exception is the degree-0 coefficient. This coefficient is set equal to zero and forced to be satisfied almost exactly, for which purpose a very low error StD is assigned to it. In this way, a global mass conservation in the Earth system is ensured (see, e.g., Croteau et al. 2021).

Since a sufficiently fine global grid is introduced to estimate EWH trends, the number of unknown parameters is relatively large ($360 \times 450 = 162{,}000$). Therefore, an explicit computation, storage and inversion of the normal matrix $(\mathbf{A}^T {\mathbf{C_d}}^{-1}\mathbf{A} + \mathbf{R})$ may be problematic. To solve this problem, we have adopted the pre-conditioned conjugate gradient method (Hestenes and Stiefel 1952). This is an iterative method, which does not require an explicit computation of the normal matrix.

3.4 Regularization

Since the number of unknown parameters by far exceeds the length of the data vector, the normal matrix in the absence of a regularization is ill-posed, so that a regularization is a must. The regularization adopted in our study stems from the assumption that mass anomalies at neighboring locations show a similar behavior. In contrast to the previous studies where a similar assumption was made (Luthcke et al. 2013; Loomis et al. 2019; Croteau et al. 2021), we strictly implement the first-order Tikhonov regularization (Tikhonov and Arsenin 1977). In this way, we avoid the need to introduce additional empirical parameters, such as

the correlation between mascons as a function of distance. The first-order Tikhonov regularization ensures the smoothness of the unknown function in terms of first derivative(s) (Ditmar et al. 2003). In practice, we implement this type of regularization by applying a discrete analog of the following minimization condition:

$$\iint_{\Omega_a} \alpha(\theta,\phi)\left[\nabla \dot{h}_w(\theta,\phi)\right]^2 d\Omega_a = \min, \tag{5}$$

where Ω_a is the sphere of radius a (the equatorial radius of the Earth); $d\Omega_a$ is an element of that sphere; $\alpha(\theta,\phi)$ is a regularization parameter ($\alpha(\theta,\phi) > 0$); $\dot{h}_w(\theta,\phi)$ is the unknown EWH trend as a function of lateral coordinates, and ∇ is the gradient operator on a sphere. This smoothness requirement is not applied along the coast lines. In other words, the regularization is not across to the pairs of neighboring cells in which one cell belongs to ocean and the other one to land. The optimal values of the regularization parameter are found in the course of a numerical study (see Sect. 4 for more detail).

3.5 Integrated mass anomalies

A soon as the EWH anomaly $(h_w)_k$ for an k-th cell has been estimated, it can be easily converted into the mass anomaly μ_k integrated over that cell:

$$\mu_k = (h_w)_k \ \rho_w \ S_k, \tag{6}$$

where ρ_w is water density (1000 kg/m^3), and S_k is the cell area. The explicit expression for the area of a rectangular cell at the surface of an ellipsoid of rotation is given in Appendix C. To obtain a regional mass anomaly integrated over a given region (e.g., Greenland), one should simply make a summation of mass anomalies μ_k over all the cells within that region. Of course, regional mass trends can be calculated similarly.

4 Data processing optimization

In order to maximize the accuracy of the estimated ice mass balance, we optimize the regularization scheme using a numerical study where an inversion of the real data is carefully reproduced. To that end, additional datasets are exploited.

4.1 Data used for the optimization

At this point, we use two additional data sets: altimetry-based and gravimetry-based.

To reproduce the EWH trends within Greenland, we use the trends in surface elevation based on Cryosat-2 altimetry data that were acquired in the time interval 2011–2015 (Simonsen and Sørensen 2017). Those trends are re-sampled onto the adopted $1^\circ \times 0.4^\circ$ grid by means of a bi-linear interpolation considering only the cells located inside Greenland. An integration over the territory of Greenland yields the trend in ice volume of -308 km^3/yr. The obtained elevation trends are converted into EWH trends by applying a constant scaling factor, so that the integration of the resulting values over entire Greenland yields -270 Gt/yr—the number that is close to the actual mass balance in Greenland in Apr. 2002–Aug. 2023, as we found in the course of preliminary computations.

To simulate realistic mass trends outside Greenland, we make use of a global high-resolution mascon solution, which was obtained by a regularized inversion of GRACE and GFO satellite data acquired between Apr. 2002 and Sep. 2020 by Loomis et al. (2021). The provided EWH trends are also re-sampled onto the $1^\circ \times 0.4^\circ$ grid adopted in our study (see the right panel in Fig. 1). The integration of the resulting EWH trends over the entire Earth's surface outside Greenland gives the total mass trend of 285.3 Gt/yr. Therefore, we scale the gravimetry-based EWH trends by applying a constant scaling factor to ensure that the result of the integration is 270 Gt/yr, which is equal to the adopted rate of mass loss in Greenland. In this way, mass conservation in the Earth system is fully reproduced.

The resulting distribution of EWH trends (the left panel in Fig. 1) is considered as the "true" signal in our numerical study. The regional mass trends obtained by the integration of the "true" signal over individual DSs, as well as over entire Greenland, are reported in the second row of Table 1.

Next, the "true" signal is converted into a set of SHC trends up to degree 120, which is consistent with the maximum degree of the primary set of real GRACE/GFO data used in our study (Sect. 2.2). The resulting signal, which has a limited spectral content, is shown in the spatial domain in the left panel in Fig. 2. To make this plot, we have used a straightforward conversion of SHC trends into EWH trends with spherical harmonic synthesis, taking the Earth's oblateness into account (Ditmar 2018). In this plot, one can clearly see, among other, fake positive trends in the inner part of Greenland, as well over the ocean along the Greenland's west coast. This is an evidence of the Gibbs phenomenon, which is triggered by the truncation of the signal spectrum in the presence of sharp spatial gradients (see also Velicogna and Wahr 2013).

Finally, the simulated SHC trends are artificially contaminated with realistic random noise. The noise realizations are generated based on error StDs that accompany the computed SHC trends (Sect. 3.1). In total, we have generated 10 noise realizations in order to make the optimization results more representative. Each of those noise realizations is added to the aforementioned "true" SHC trends. The signal contaminated by one of those realizations is shown (again, in the

Table 1 Results of the numerical study aimed at the optimization of the data processing scheme (Gt/yr): the "true" regional mass trends (second row) and the RMS recovery errors after the optimal inversion of 10 realization of noisy data (last row)

DS	N	NW	W	SW	SE	NE	RMS	Entire Greenland	Composed error
"True" regional mass trend	−35.4	−66.4	−58.7	−68.6	−41.8	0.9	–	−270.0	–
Recovery error (RMS)	1.6	0.5	0.5	1.1	2.2	0.9	1.3	0.8	1.5

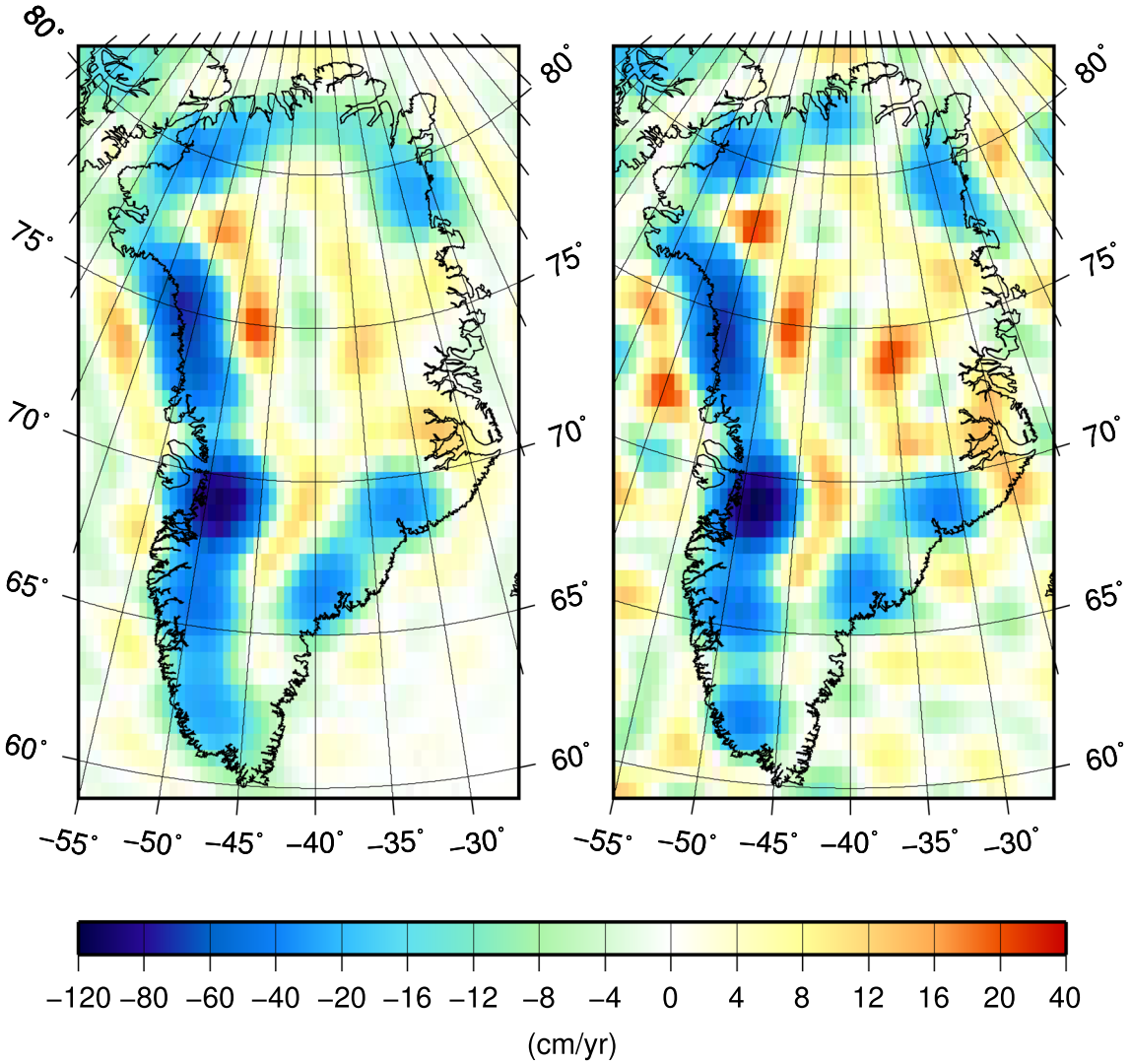

Fig. 2 EWH trends considered in the numerical study after limiting their spectrum to maximum degree 120: noise-free signal (left) and a realization of noisy signal (right). The degree-1, $\dot{\bar{C}}_{2,0}$, and $\dot{\bar{C}}_{3,0}$ coefficients are eliminated in the latter case

spatial domain) in the right panel in Fig. 2. In making this plot, we have ignored the degree-1, $\dot{\bar{C}}_{2,0}$, and $\dot{\bar{C}}_{3,0}$ coefficients for the sake of consistency with the primary set of real data (Sect. 2.2).

4.2 Data inversion

Realizations of noisy SHC trends are inverted into EWH trends on a global 1° × 0.4° grid, as it is explained in Sect. 3.2–3.4. In each inversion run, four values of regularization parameter $\alpha(\theta, \phi)$ are pre-defined: (i) over ocean; (ii) over land outside Greenland; (iii) over the Greenland's

coastal areas (i.e., the region outside the inner part of the GrIS); and (iv) over the inner part of the GrIS. The latter regularization parameter value applies to all the pairs of neighboring cells that are located at the distance larger than 80 km from the GrIS margin. It is believed that the latter value must be much larger than the one applied to the Greenland's coast. This is because mass changes in the inner part of the GrIS are characterized by a much weaker spatial variability than in the rest of Greenland (Ewert et al. 2012). Noteworthy, we apply a minor adjustment to the actual geometry of coast lines worldwide, so that small isolated pieces of land (i.e., islands) and of ocean are eliminated.

4.3 Optimization procedure

The goal of the optimization is to define the regularization scheme that ensures the best mass balance estimates, both for individual DSs and for entire Greenland. To that end, the differences between the recovered and "true" regional mass trends are considered after each inversion run. The regional difference over the kth DS, $\delta\dot{M}_k$, is computed, in line with Sect. 3.5, with a discrete variant of the following expression:

$$\delta\dot{M}_k[Gt/yr] = 10^{-12}\cdot\rho_w \iint\limits_{\Omega_k}\left[\hat{\dot{h}}_w(\theta,\lambda)-\dot{h}_w(\theta,\lambda)\right]d\Omega, \tag{7}$$

where Ω_k is the territory of the kth DS, ρ_w is water density in kg/m^3, $\hat{\dot{h}}_w(\theta,\lambda)$ and $\dot{h}_w(\theta,\lambda)$ is the recovered and the "true" EWH trend, respectively (in m/yr), and $d\Omega$ is the area of an element at the surface of the reference ellipsoid (in m^2).

Various values of the regularization parameter in the four aforementioned zones are tried in the course of the optimization. The goal is to find the values for which the following quantity is the smallest:

$$\delta\dot{M}_{comp} = \sqrt{\left(\delta\dot{M}_{RMS}\right)^2+\left(\delta\dot{M}_{Greenland}\right)^2} = \min, \tag{8}$$

where $\delta\dot{M}_{RMS}$ is the RMS difference between the recovered and the true regional mass trends per DS:

$$\delta\dot{M}_{RMS} = \sqrt{\frac{1}{6}\sum_{k=1}^{6}(\delta\dot{M}_k)^2}, \tag{9}$$

whereas $\delta\dot{M}_{Greenland}$ is the error in the regional mass trend estimated for entire Greenland:

$$\delta\dot{M}_{Greenland} = \sum_{k=1}^{6}\delta\dot{M}_k. \tag{10}$$

Thereafter, the value $\delta\dot{M}_{comp}$ is termed "composed error". Each of the 10 realizations of noisy data is used to find the optimal regularization parameter values using the coordinate descent algorithm. The values vary in the logarithmic scale with a step of about $10^{\frac{1}{2}}$.

4.4 Optimization results

In line with the explanations in Sect. 4.2, four optimal values of regularization parameter $\alpha(\theta,\phi)$ had to be defined. The optimal values for the ocean, land outside Greenland, and the inner part of the GrIS, are found as 3×10^6, 3000, and 300, respectively (these values yield the smallest composed error for 6 realizations of noisy data out of 10). As far as the regularization parameter value for the Greenland's coast is concerned, the composed error turns out to be insensitive to it, provided that it is sufficiently small. In what follows, the regularization parameter is set there equal to 10^{-4}.

The EWH trends obtained with the optimal regularization parameter values from noisy data are shown in the right panel in Fig. 3. To be more specific, the realization of noisy data demonstrated in the right panel in Fig. 2 is addressed. For a comparison, the EWH trends obtained with the same regularization scheme from the noise-free data is shown in the left panel in Fig. 3. The results are surprisingly close to each other; the impact of random errors is hardly visible. One may also notice significant positive trends at a few locations (particularly, along the northern coast). Most probably, these are artefacts occurred due to an amplification of errors in the presence of a weak regularization along the coast. Apparently, these artefacts are averaged out when EWH trends are integrated over DSs, so that a stronger regularization is not needed when the goal is to obtain the best estimates of *regional* mass trends.

The RMS recovery errors obtained after the inversion of 10 realization of noisy data with the optimal regularization scheme are reported in the last row in Table 1. One can see that the optimal regularization parameters ensure a high accuracy of the recovered trends: the recovery errors are of the order of 1–2 Gt/yr or, in some cases, even less.

5 Noise budget of the estimates obtained with the optimal data processing scheme

The focus of this section is a comprehensive analysis of the noise budget, when the optimized data processing scheme is applied to real GRACE/GFO data. We consider the following contributors: (1) random noise; (2) signal leakage; (3) GIA model uncertainties; (4) raw data processing uncertainties; and (5) data weighting uncertainties in the context of trend estimation. To make the results more objective, all the input

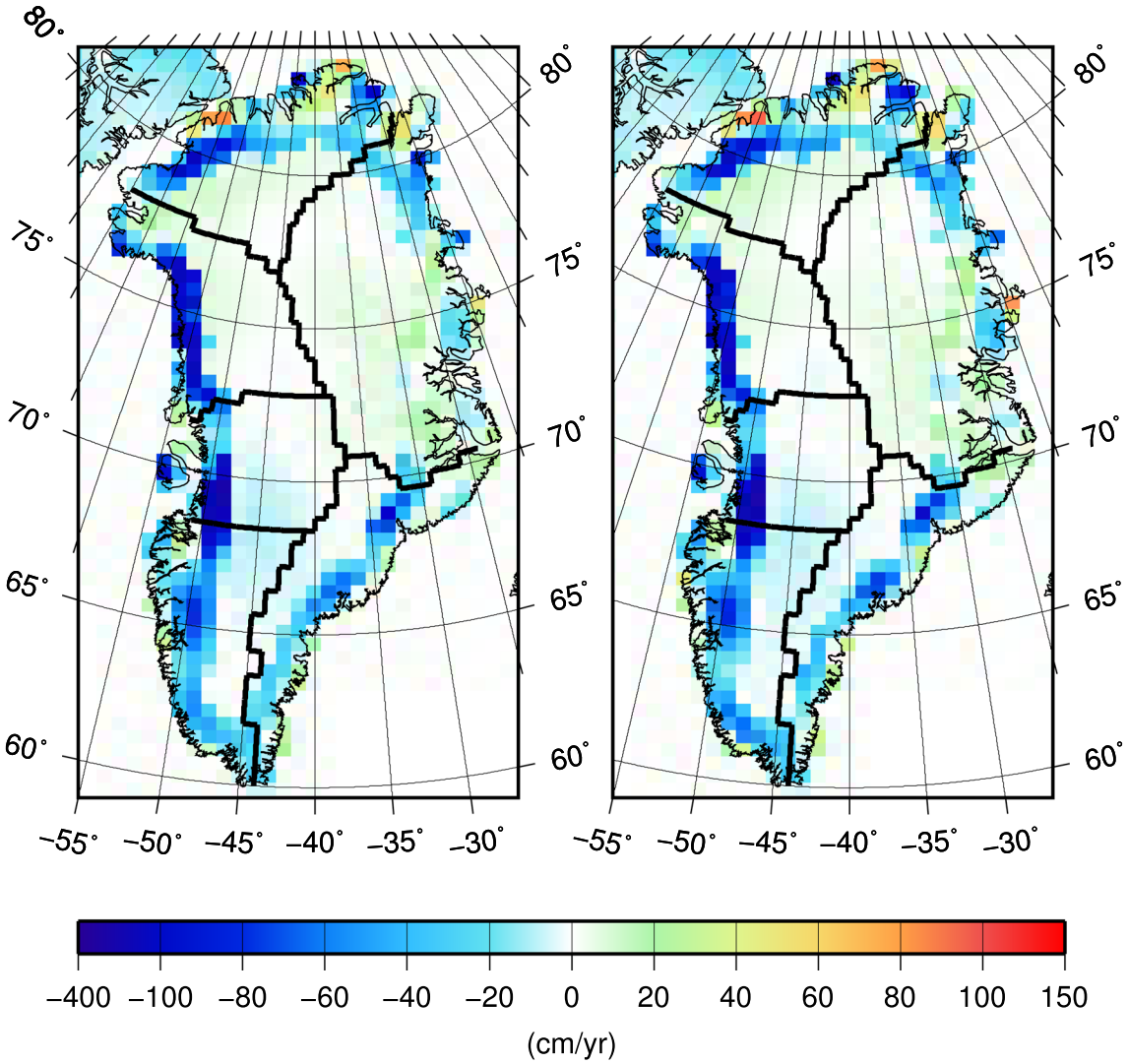

Fig. 3 EWH trends recovered in the numerical study with the optimal regularization scheme from noise-free data (left panel) and from the realization of noisy data shown in the right panel in Fig. 2 (right panel)

data considered in this section are different from those used in the optimization of the data processing scheme addressed above.

5.1 Random noise

In the first instance, random noise in SHCs reflects errors in the data collected by sensors onboard GRACE and GFO satellites. At the same time, processing those data includes a subtraction of signals caused by rapid mass transport processes. Background models used for that purpose suffer from their own errors, which manifest themselves as additional random noise in SHCs. Therefore, an empirical calibration of error StDs supplying SHCs is needed to ensure that this additional noise is taken into account. To check if that is the case in the context of ITSG-Grace2018 solutions, we compare the error StDs propagated into SHC trends with the SHC trends themselves in terms of geoid height per degree (Fig. 4). In the range of low degrees, the degree amplitude of SHC trends decreases with degree, which is a typical behavior of mass transport signals (Wahr et al. 1998). At higher degrees, however, the role of random errors keeps increasing, so that those errors ultimately become the dominant contributor to the observed degree amplitudes (Sasgen et al. 2006). One can see that the error StDs propagated into SHC trends indeed become close to the SHC trends in the range of highest degrees. This is exactly the expected behaviour when the provided error StDs are properly calibrated.

To analyse the contribution of random noise to the noise budget, we generate 10 new realizations of random errors in SHC trends in the same way as we did in the course of data processing optimization (Sect. 4.1). Those error realiza-

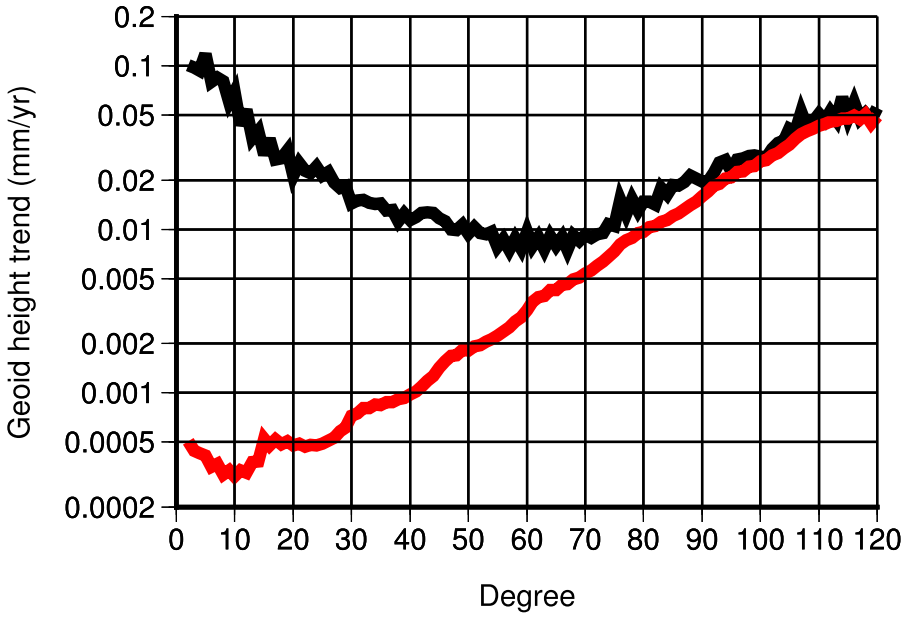

Fig. 4 Trends derived from ITSG-Grace2018 monthly SHCs (black curve), as well as the associated error StDs (red curve), in terms of geoid height per degree

tions are added to the "true" SHC trends generated in that section. The sets of noisy SHC trends obtained this way are inverted into EWH trends using the optimal regularization scheme. The resulting EWH trends are very similar to those presented earlier in Fig. 3, which confirms that the impact of random errors in the data is small. Finally, we compute the differences between the recovered noisy EWH trends and the "noise-free" EWH trends, which are obtained on the basis of the noise-free SHC trends with the same regularization scheme. The RMS differences obtained by averaging over all 10 realizations of noisy data are presented in the left panel in Fig. 5. The highest noise level is observed in the region where the applied regularization is weakest, i.e., along the Greenland coast.

The regional trend differences integrated over individual DSs and the resulting RMS values, as well as the regional differences integrated over entire Greenland are reported in Table S.1 in Supplementary material. Furthermore, that table presents the corresponding RMS values based on all the 10 realizations of noisy data. Those RMS values are also shown in the second row in Table 2 as a contribution of random noise to the overall noise budget. One can see that the contribution of random noise is indeed minor: it does not exceed 1 Gt/yr in most of cases.

5.2 Signal leakage

The primary cause of "signal leakage" in the context of satellite gravimetry is a limited spectral content of the collected data. Then, it is common to make an implicit assumption that signal in the SHCs above certain maximum degree is zero. This results in a Gibbs phenomenon (or "ringing artefacts") when SHCs are converted into signal in the spatial domain with the spherical harmonic synthesis (this could also be seen in the left panel in Fig. 2). Very similar results are also obtained with the least-squares adjustment when the applied constraints are reduced to minimum (namely, when a small regularization parameter is applied uniformly, without distinguishing different regions, including land and ocean). The goal of the applied constraints (such as those based on the geometry of coast lines) is to mitigate the signal leakage by implicitly introducing high-degree information, which is absent in the original data. Unfortunately, this cannot eliminate the signal leakage entirely.

All the results obtained in the course of the optimization were based on the same "true" signal derived from Cryosat-2 data collected in 2011–2015 (Fig. 1, left panel). Of course, that signal is different from actual EWH trends in the entire time interval we consider (Apr. 2002–Aug. 2023), so that the signal leakage occurred in the course of the optimization cannot be considered as sufficiently representative. To make an independent and a more representative assessment of possible signal leakage, we generate several alternative signal realizations based on estimates of elevation trends in Greenland. More specifically, we consider the estimates based on multiple satellite altimetry data collected over four time intervals: 2003–2007, 2007–2011, 2011–2015, and 2015–2019 (Sørensen et al. 2018). As before, we convert each elevation trend distribution into EWH trend distribution by applying a constant scaling factor such that the rate of total mass loss in Greenland is equal to 270 Gt/yr. Most of the exploited trend estimates imply relatively low rates of total ice volume

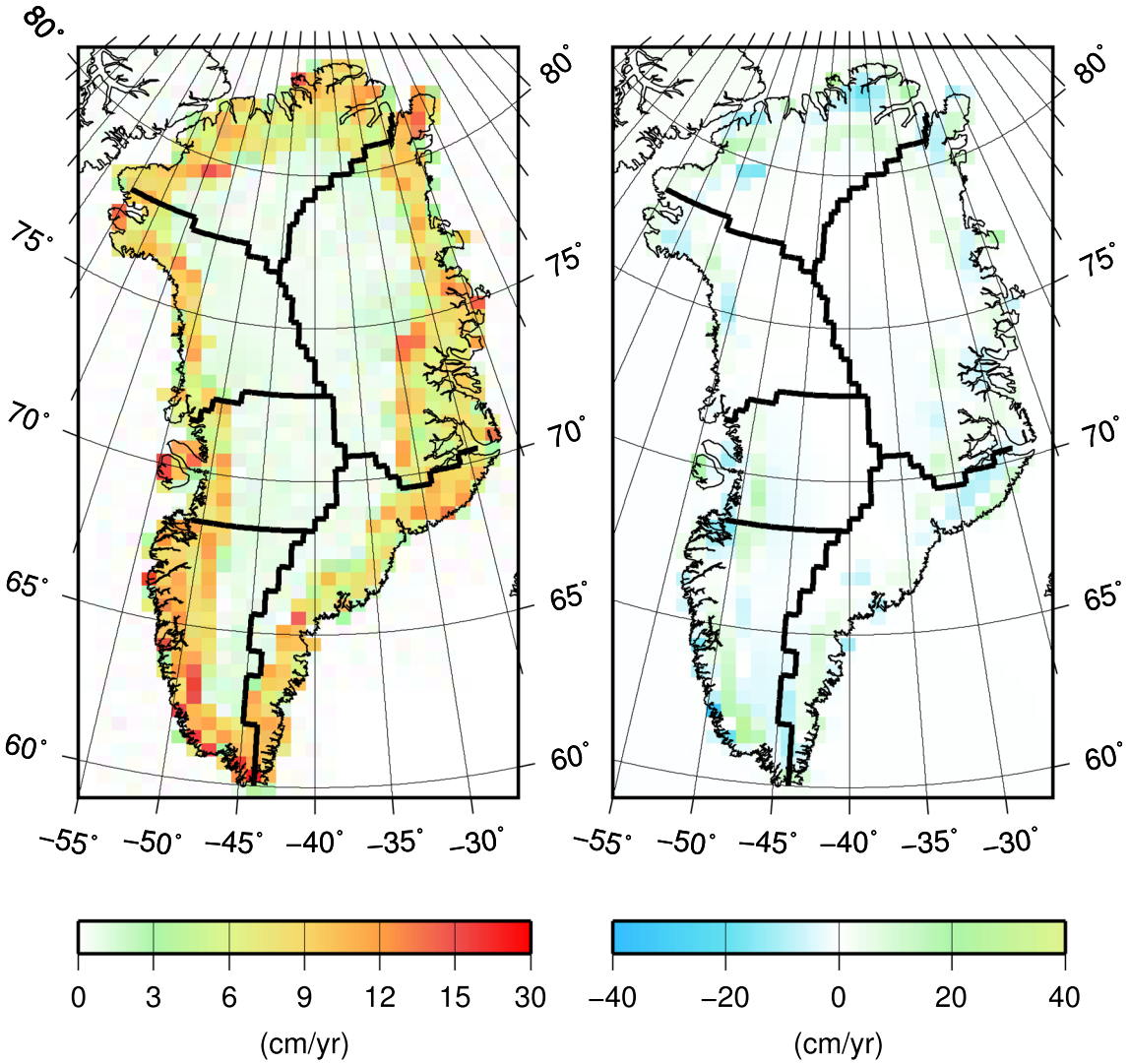

Fig. 5 Numerical study, analysis of contributors to the noise budget of recovered EWH trends: RMS random errors obtained by averaging over all 10 noise realizations under consideration (left) and GIA model uncertainty defined as 50% GIA signal (right)

Table 2 Noise budget of the regional trend estimates (Gt/yr)

Noise budget contributor\DS	N	NW	W	SW	SE	NE	RMS	Entire Greenland
Random noise (RMS)	0.7	0.4	0.6	0.9	1.4	1.0	0.9	0.3
Signal leakage (RMS)	2.1	0.6	2.8	2.8	4.7	2.3	2.8	0.7
	(2.0)	(0.6)	(2.9)	(2.7)	(4.9)	(2.0)	(2.8)	(2.1)
GIA uncertainty	4.2	0.7	0.2	0.02	1.0	3.0	2.2	9.1
Raw data processing uncertainty (RMS)	0.6	1.1	0.2	2.5	3.8	1.5	2.0	3.5
Data weighting uncertainty (RMS)	0.4	0.6	0.1	3.4	2.9	0.5	1.9	1.0
Total	4.9	1.6	2.8	5.2	7.0	4.2	4.6	9.9

The numbers in parentheses in row "Signal leakage" were obtained when low-degree SHCs were included into the input data vector (those numbers were not considered in the calculation of the total noise budget)

loss in Greenland: 158, 186, 233, and 81 km^3/yr in 2003–2007, 2007–2011, 2011–2015, and 2015–2019, respectively. Therefore, the applied scaling factor is in some cases relatively large. This implies that the obtained estimates of signal leakage may be rather conservative. The resulting realizations of alternative signal are shown in Fig. S.1 in Supplementary material.

Each of these alternative signal realizations is treated similarly to the "true" signal in the course of optimization (Sect. 4.1): it is combined with GRACE/GFO-based EWH trends outside Greenland (Loomis et al. 2021) and converted into SHCs up to degree 120. After that, each of these noise-free sets of SHC trends is inverted into a global distribution of EWH trends using the optimal regularization scheme. Each of the obtained results is compared with the corresponding "true" signal in terms of regional mass trends obtained by the integration over individual DSs and entire Greenland (Table S.2). The RMS differences between the recovered and "true" trends obtained by averaging over all 4 signal realizations are considered as an estimate of signal leakage in general (in the context of the selected regularization scheme); they are reported also in the third row in Table 2. It can be seen that the resulting signal leakage is at least an order of magnitude smaller than the total signal (regional mass trend) in most of cases (see Table 1). An exception is NE drainage system, where the regional mass trend is minor.

We have also used the alternative signal realizations to assess the role of the low-degree SHCs, which are ignored by default in our study (see Sect. 2.2). In the case of a spherical harmonic synthesis, an omission of low-degree SHCs may result in a noticeable disturbance of the obtained results, especially if regional mass trends are integrated over large areas (Swenson et al. 2008). In contrast, the least-squares adjustment exploits these coefficients as just a few additional elements in the input data vector. Incorporation of those coefficients may or may not play an important role, depending, among other, on the weights assigned to those coefficients. In our study, we have defined those weights on the basis of error StD per low-degree SHC trend. In line with the other SHCs, we have estimated these error StDs by means of the conventional error propagation (see Sect. 3.1). As input, the error StDs provided together with the low-degree SHCs themselves have been used; see (Sun et al. 2016) for degree-1 SHCs and (Loomis et al. 2020) for $C_{2,0}$ and $C_{3,0}$.

The signal leakage obtained in the presence of low-degree trends in the data vector is reported in Table S.2 in parentheses, both per signal realization and as RMS values based on all 4 realizations. Furthermore, the resulting RMS values are shown in parentheses in the third row in Table 2. One can see that the incorporation of the low-degree trends has resulted in only marginal changes in the regional mass trends integrated over individual DSs. As far as entire Greenland is concerned, incorporation of the low-degree trends results in a minor but systematic underestimation of the mass loss rate (by about 2 Gt/yr). Most likely, this is because of an inconsistency between the conducted data processing optimization and the set-up of input dataset. As it is explained above, the data processing scheme has been optimized for the input data vector without low-degree trends. Apparently, incorporation of those trends into the set of input data results in a minor additional signal leakage, making the selected regularization scheme somewhat sub-optimal. In what follows, we proceed with the datasets that lack the low-degree trends.

5.3 GIA model uncertainties

In the context of ice mass balance estimation, the SHC trends based on real GRACE/GFO data have to be cleaned from GIA signal. The models used for that purpose are characterized by their own uncertainties, which also contribute to the noise budget of the resulting estimates. In our study, ICE-6G model is used (Sect. 2.2). As a conservative estimate, we define its uncertainty as 50% of the GIA signal itself. To quantify the contribution of this uncertainty to the error budget, we add 50% of the GIA signal to the noise-free SHC trends based on the "true" signal used in the optimization (Fig. 2, left panel), invert it into EWH trends, and subtract the result of inversion of noise-free SHCs alone (Fig. 3, left panel). The resulting differences are shown in the right panel in Fig. 5. The GIA-related distortions are concentrated in the coastal areas (where the regularization is weakest) and are significantly smaller than the total signal, which is shown in Fig. 2. Nevertheless, after an integration over individual DSs, the average contribution of GIA-related uncertainties to the noise budget typically exceeds the contribution of random noise and is comparable to the contribution of signal leakage, as it is shown in the fourth row in Table 2. For two DSs ("N" and "NE"), as well as for entire Greenland, the contribution of GIA uncertainties even plays the dominant role.

5.4 Raw data processing uncertainties

The SHC estimates produced by different data processing teams are slightly different, even if the same raw (level-1b) GRACE/GFO data and background models are used. Assuming that all the adopted data processing schemes are flawless, one can explain this by differences in those schemes themselves. This may include different variants of outlier detection and data weighting, as well as different approaches to the co-estimation of various empirical parameters, such as accelerometer calibration parameters. Thus, differences between the solutions from different data processing teams can be seen as a way to *indirectly* assess the impact of noise in raw data and background models. In what follows, these differences are termed "raw data processing uncertainties".

Table 3 GRACE/GFO data products exploited to quantify the raw data processing uncertainties and data weighting uncertainties

Data processing team	Acronym used in this study	Release of Grace data	Release of GFO data	Maximum spherical harmonic degree	References
German research Centre for Geosciences in Potsdam (Germany)	GFZ	RL06	RL06.1	96	Dahle et al. (2018)
Jet Propulsion Laboratory of the California Institute of Technology (USA)	JPL	RL06	RL06.1	96	Yuan (2018)
Institute of Geodesy at Graz University of Technology (Austria)	ITSG	Grace2018	Grace2018	96	Kvas et al. (2019)

Importantly, these uncertainties are independent of information about the accuracy of the SHCs provided by the data processing teams themselves, so that there is no risk of a noise underestimation if that information is too optimistic. As a conservative assumption, we consider the raw data processing uncertainties as an additional contributor to the noise budget, which does not replace the estimates of random noise addressed in Sect. 4.4. We refrain from an elimination of explicitly estimated random noise contribution due to the fact that raw data processing uncertainties may theoretically underestimate the impact of random errors. Indeed, if different data processing teams adopt very similar data processing schemes, their results will also be very similar, independently of the the actual noise levels in raw data and background models.

To quantify the raw data processing uncertainties, we consider three GRACE/GFO data products: GFZ, JPL, and ITSG (see Table 3 for more detail). As before, each data product consists of monthly sets of SHCs. It is worth noticing that the data products used in this comparison are complete to degree 96 only. This is because GFZ and JPL data products complete to degree 120 do not exist. We take care that data gaps in the GFZ, JPL, and ITSG time-series are identical (that is, if a particular month is absent in a given time-series, this month is also not included into the other time-series).

Each time-series is used to estimate the linear trend per SHC, as it is explained in Sect. 3.1. The result (after the conversion into the spatial domain) is shown in three out of four panels in supplementary Fig. S.2. A similarity of the three trend estimates implies that the effect of random noise in all three is minor, which is consistent with the findings of Sect. 4.4. The fourth (bottom right) panel shows similar trend estimated from CSR RL06/RL06.3 data product (Bettadpur 2018). Unfortunately, this estimate clearly shows a significantly higher noise level (particularly, in the southern part of the region shown), the origin of which is unclear to us. For this reason, it is decided not to consider the CSR data product in the comparison for the time being.

The SHC trends based on the ITSG, GFZ, and JPL data products are inverted into EWH trends with the optimal regularization scheme. The weights assigned to SHC trends are also the same as those considered in the optimization (the degrees higher than 96 being ignored). This makes the inversion results more consistent both with the applied optimization and with each other (even though this may cause a deviation of a result from the statistically-optimal one). The results based on the three data products, as well as the mean of them, are shown in Fig. 6. Inversion of real ITSG data results in EWH trends that are remarkably similar to those we observed in the numerical study (Fig. 3), which is an indication that our numerical study was indeed sufficiently realistic. The other two show a higher noise level, which manifests itself, among other, as fake positive trends here and there (they are particularly prominent in the GFZ-based solution). This is consistent with our earlier finding that noise levels in JPL and GFZ solutions somewhat exceed that in ITSG solutions (Ditmar 2022, Table 4).

The integration of EWH trends over individual DSs and over entire Greenland yields the regional mass trends reported in Table 4. This table shows that all three GRACE/GFO data products result in rather similar estimates. An exception is GFZ-based estimates for two DSs: N, and NE. In these two DSs, the GFZ-based regional mass loss estimate is respectively weaker and stronger than the other two data products suggest. A visual inspection of the corresponding EWH trends (top right panel in Fig. 6) reveals a likely cause of these deviations. The border between the north and northeast DSs crosses an anomalous feature consisting of a positive and a negative anomaly. This feature is likely an artifact caused by a very weak regularization in the coastal zone. Unfortunately, an integration over DSs does not average out this artifact because its positive lobe happens to be in the north and the negative one in the northeast DS. Thus, the statistics

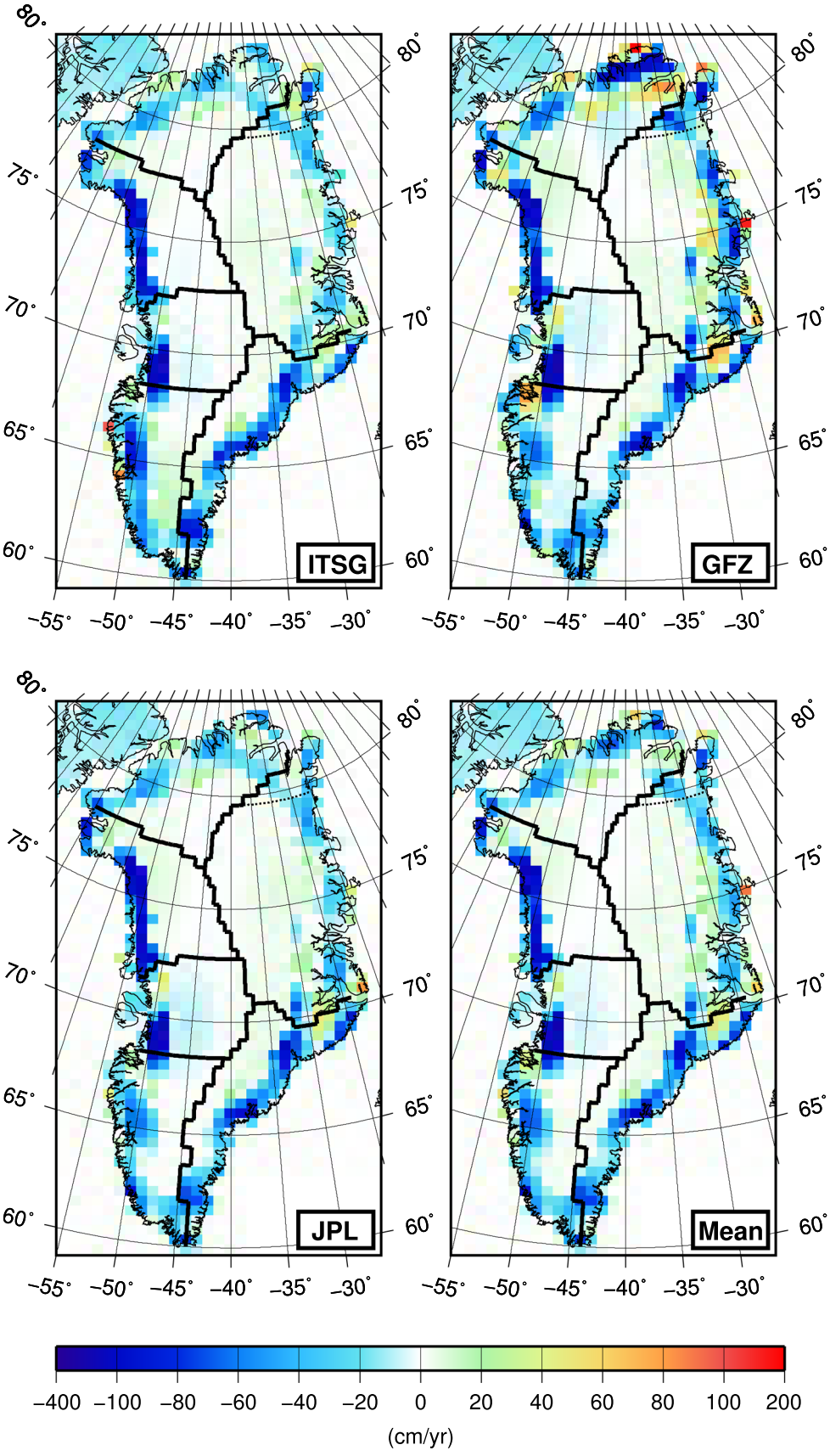

Fig. 6 EWH trends obtained by the inversion of SHC trends based on level-2 GRACE/GFO data products from ITSG, GFZ, and JPL, as well as the mean of the three estimates. The dashed line at 79.6°N latitude depicts an adjusted border between the north and northeast DSs (see the main text for more information)

Table 4 Comparison of regional mass trends based on alternative GRACE/GFO data products, which are complete to degree 96 (see Table 3)

GRACE/GFO data product\DS	N	NW	W	SW	SE	NE	RMS	Entire Greenland
ITSG	−28.1	−64.9	−36.8	−44.0	−77.6	−19.4		−270.8
	(−36.1)					(−11.4)		
GFZ	−18.1	−67.0	−36.5	−48.2	−70.0	−26.1		−265.8
	(−35.2)					(−9.0)		
JPL	−29.0	−66.1	−36.4	−48.3	−73.8	−19.0		−272.5
	(−36.4)					(−11.5)		
Mean	−25.1	−66.0	−36.6	−46.8	−73.8	−21.5		−269.7
	(−35.9)					(−10.6)		
StD	6.0	1.1	0.2	2.5	3.8	4.0	3.5	3.5
	(0.6)					(1.5)	(2.0)	

The trends integrated over DSs individually and over entire Greenland are shown. The numbers reported in parentheses are obtained after an adjustment of the border between the north and northeast DSs (see the main text for more information). Just those numbers are used to quantify the contribution of raw data processing uncertainties to the overall noise budget. Units: Gt/yr

presented in Table 4 is significantly biased by this artifact in the GFZ solution and is likely not representative of errors in ITSG solutions, which are the subject of our primary interest. To mitigate the impact of this artifact, we slightly move the border between the north and northeast DSs southwards (the new border geometry is shown in Fig. 6 with a dashed line). The regional mass trends obtained after this adjustment are reported in Table 4 in parentheses. Obviously, the adopted adjustment substantially reduces the difference between the estimated regional mass trends in the two DSs. We use the statistics obtained after the border adjustment to quantify the contribution of the raw data processing uncertainties to the overall noise budget (see the fifth line in Table 2).

The raw data processing uncertainties are relatively small: not more than 1.5 Gt/yr for the northern DSs (N, NW, W, and NE) and of the order of 3 Gt/yr for the southern ones (SW and SE), as well as for entire Greenland. The RMS value in the context of DS-related regional mass trends is 2.0 Gt/yr.

Though the estimated uncertainties are rather small, they are larger than the explicitly estimated contributions of random errors (see the second line in Table 2). To some extent, this can be explained by a relatively low noise level in the ITSG data product (Ditmar 2022). Thus, the revealed differences between the data products mostly reflect the noise level not in the ITSG data product, but in the other two. Furthermore, the conducted comparison deals with GRACE/GFO sets of SHCs complete to degree 96 only. Thus, the total number of elements in the data vector $\mathbf{d}$ composed of SHC trends (Eq. 4) is about 9,400. On the other hand, a SHC set complete to degree 120, which was considered in the numerical study, increases the length of the data vector by more than 5000 elements. Even though these additional data are relatively noisy, such a large number of additional data may somewhat increase the accuracy of inversion results. Some random fluctuations could also have affected the outcome of the conducted comparison of GRACE/GFO data products (one can see the potential effect of such fluctuations by comparing the results obtained with the original and the adjusted border between the north and northeast DSs). Finally, it cannot be excluded that the conducted numerical study did not fully reproduce the actual stochastic behaviour of data errors. This highlights the need in the indirect quantification of random errors—as raw data processing uncertainties, let the obtained results be somewhat conservative.

5.5 Data weighting uncertainties

As it is explained in Sect. 3.1, the SHC trends are estimated on the basis of functional model given by Eq. (1), with the statistically-optimal data weights defined in line with the error StDs that accompany the provided GRACE/GFO monthly solutions. If those error StDs are subject to long-term variations, such an approach may result in a biased trend estimation, provided that the SHC trends themselves also show inter-annual variations. For instance, relatively high weights assigned to the data within a time interval of rapid mass loss may result in a trend overestimation and vice versa. At the same time, long-term variations in the reported data accuracy are definitely not excluded, which can be both due to variations in the quality of raw data and due to changing satellite orbit altitudes.

To illustrate this statement, we have computed the total (formal) error of each monthly solution in terms of geoid heights:

$$\sigma_{total} = R_E \sqrt{\sum_{l=2}^{96} \sum_{m=-l}^{l} \sigma^2 \left(\bar{C}_{l,m}\right)}, \tag{11}$$

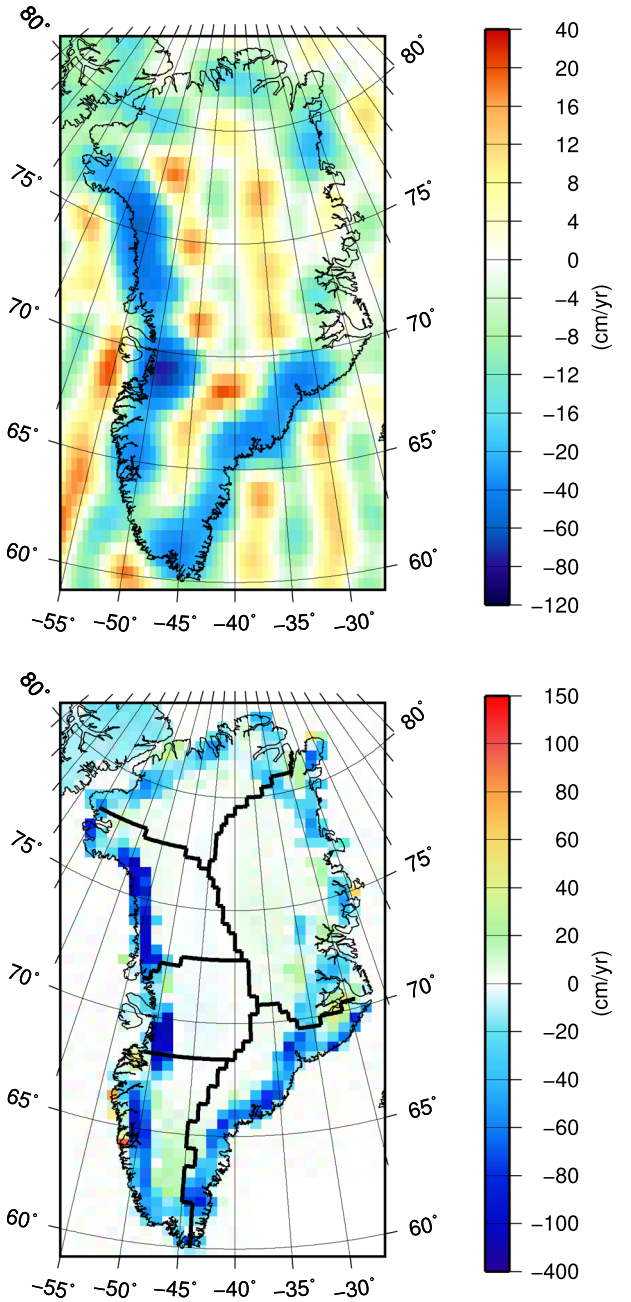

Fig. 7 Processing real GRACE/GFO data: the input for the regularized inversion, i.e. SHC trends up to degree 120 obtained from monthly ITSG solutions, after an elimination of low-degree coefficients and conversion into the spatial domain with the spherical harmonic synthesis (Ditmar 2018) (top) and the results of the regularized inversion with the optimized regularization scheme (bottom)

where R_E is the Earth's radius, and $\sigma\left(\bar{C}_{l,m}\right)$ are the provided error StDs per SHC. The time-series of calculated total errors are presented in supplementary Fig. S.3. Apart from a short-term variability, which likely plays little role, one can clearly see the presence of long-term variations in the total errors. For instance, all the solutions show a reduction in the total error in 2010–2016, which is most likely due to a steadily decreasing altitude of GRACE satellites in this time interval.

To quantify this uncertainty, we have re-used the monthly solutions from ITSG, GFZ, and JPL introduced in the previous section. These solutions are exploited again to compute SHC trends in line with the functional model given by Eq. (1). Two variants of the SHC trends are considered: the ones obtained with the statistically-optimal weights and those estimated with the ordinary least-squares adjustment (i.e., without applying time-varying weights). The regional mass trends obtained on the basis of both variants, as well as the differences between them, are reported in supplementary Table S.3. We consider the RMS differences based on all three GRACE/GFO data products as a measure of the data weighting uncertainties in the context of trend estimation; these uncertainties are also reported in the 6th line in Table 2. Of course, this is a conservative estimation, since the obtained differences reflect not only bias in the estimated trends, but also an increase in their noise levels when the estimation procedure lacks statistically-optimal data weighting.

One can see that the data weighting uncertainties stay at sub-Gt/yr level in most of cases. However, in the south part of Greenland (in SW and SE drainage systems), they are several times larger (of the order of 3 Gt/yr). Thus, their spatial variability is similar to that of raw data processing uncertainties addressed in the previous section.

5.6 Noise budget: the summary

Our estimates of total errors in the regional mass trends are reported in the last row of Table 2. We have calculated them as root-sum-squares of individual contributors to the noise budget, assuming that those contributors are not cross-correlated. These errors are sufficiently low: 4.6 Gt/yr (RMS) for individual DSs and about 10 Gt/yr for entire Greenland. The largest total errors (5 to 7 Gt/yr) are found for the southern DSs (SW and SE) due to an increased level of both raw data processing uncertainties and data weighting uncertainties. This is not very surprising, since it is well known that the accuracy of satellite gravimetry decreases towards the equator (due to both less data per unit area and less favourable observations conditions when the ascending and descending orbit tracks become nearly parallel).

6 Results

6.1 Definitive estimates of regional mass trends in Greenland

The definitive estimates of regional mass trends in Greenland are based on the primary set of GRACE/GFO monthly solutions: the ITSG solutions complete to spherical harmonic

degree 120 (Sect. 2.2). To visualize the SHC trends estimated on the basis of these solutions, we have converted them into the spatial domain using the spherical harmonic synthesis (Ditmar 2018), see the top panel in Fig. 7. The result of the data inversion with the optimal regularization scheme is presented in the bottom panel in the same figure. The regional mass trend estimates integrated over individual DSs and over entire Greenland, as well as the corresponding errors, are reported in the second and third raw in Table 5, respectively. The overall rate of mass loss in Greenland in the considered time interval (Apr. 2002–Aug. 2023) is estimated, roughly speaking, as 271 $\pm$ 10 Gt/yr. The largest rates of mass loss—above 65 Gt/yr—are observed in NW and SE DSs. In contrast, NE drainage system demonstrates a relatively stable behavior: the rate of mass loss there is less than 20 Gt/yr. Importantly, the obtained estimates are characterized by a high accuracy (of the order of 5 and 10 Gt/yr for individual DSs and entire Greenland, respectively). This ensures sufficiently high SNRs not only for entire Greenland, but also for all the DSs (between 5 for NE and 42 for NW, see the last row in Table 5).

One may notice that the estimated rate of the total mass loss in Greenland ($\approx$ 271 Gt/yr) is very close to the one adopted in the optimization of the data processing scheme in Sect. 4 (270 Gt/yr). This is explained by the fact that a similar rate was obtained already in the course of preliminary computations, when the value used in the optimization was somewhat larger (290 Gt/yr). On the basis of those preliminary computations, it was decided to re-do the optimization using the rate of 270 Gt/yr to avoid an overestimation of the signal leakage. Thus, a similarity of the two numbers must be seen as an evidence of a convergence of our computations, and not as a bias towards the value used in the optimization.

A comparison of the SHC trends shown in the top panel in Fig. 7 with similar trends addressed in the previous two sections (Fig. S.2, top left panel) shows a significant amplification of noise, which can be explained by the contribution of SHCs above degree 96. Nevertheless, a comparison of the regional mass trends based on the primary data set with those estimated for the same geometry of DSs in the previous two sections from ITSG data (Table 4, second row) shows that changing the maximum degree from 96 to 120 results in only minor changes (within $\approx$ 1 Gt/yr), when the optimized data processing scheme is applied. The observed changes can be explained, for instance, by a reduced signal leakage in the presence of high-degree SHCs. An increase in the number of input data could also have played a role due to an increase in the accuracy of the resulting estimates (see also the discussion at the end of Sect. 5.4).

6.2 Robustness of the obtained estimates

In this section, we investigate to what extent the obtained trend estimates depend on possible modifications in the data processing. The following factors are addressed: (i) usage of more monthly solutions as input; (ii) including low-degree SHC trends into the input dataset; (iii) estimation of SHC trends without data weighting; and (iv) approximation of the Earth's surface with a sphere rather than with the reference ellipsoid.

As it is mentioned in Sect. 2.2, nine monthly solutions are omitted in the primary set of input data. To quantify the effect of this omission, we have repeated the computation of SHC trends with a subsequent inversion into regional mass trends, having included those monthly solutions. The obtained results, as well as the differences with respect to those based on the primary dataset, are reported in the 2nd and 3rd row of Table 6. One can see that the omission of nine monthly solutions have had only a minor effect in the context of individual DSs (not more that 0.2 Gt/yr) and a negligible effect in the context of entire Greenland.

Next, we have considered the effect of including low-degree SHC trends into the input data vector. We remind that this concerns five SHCs: three degree-1 coefficients, $C_{2,0}$, and $C_{3,0}$. Table 6 (rows 4 and 5) shows that this changes the mass balances estimated for individual DSs by less than 1 Gt/yr. However, the mass balance of entire Greenland is reduced in this way by 2.6 Gt/yr. We remind that a very similar effect was observed in the context of our numerical study, when an incorporation of low-degree SHC trends into the data inversion resulted in an underestimation of the Greenland's mass balance by about 2 Gt/yr (see the discussion at the end of Sect. 5.2). We interpret this as an evidence of an additional signal leakage caused by a mismatch with respect to the set-up adopted in the optimization. Most probably, we see the same effect in the context of real data. In any case, a reduction of the Greenland-wide trend by 2.6 Gt/yr stays within the estimated error margins.

One may find it counter-intuitive that an accurate recovery of mass anomalies is achievable even in the absence of low-degree SHCs. Indeed, those coefficients contain important information about the large-scale behavior of the signal of interest. In the absence of those SHCs, mass anomalies recovered with a straightforward spherical harmonic synthesis may suffer from noticeable distortions. In our case, however, recovery of mass anomalies takes place in a totally different way—with a regularized least-squares adjustment. Then, a proper choice of the regularization scheme allows one to use available prior information about the unknown function to compensate the absence of low-degree SHCs. To illustrate this statement, we have considered a simple numerical example where a 1-D function is recovered from its incomplete spectrum using a regularized least-squares

Table 5 Definitive estimates of regional mass trends in Greenland in Apr. 2002–Aug. 2023 obtained with the proposed data processing scheme (2nd row), as well as the their accuracy (3rd row) and signal-to-noise ratio (last row)

DS	N	NW	W	SW	SE	NE	RMS	Entire Greenland
Regional mass trend (Gt/yr)	− 28.3	− 65.1	− 37.9	− 43.8	− 76.6	− 19.3	–	− 270.9
Error StD (Gt/yr)	4.9	1.6	2.8	5.2	7.0	4.2	4.6	9.9
SNR	6	42	13	8	11	5	19	27

The primary data GRACE/GFO product, which is complete to degree 120, is used as input

Table 6 Estimates of regional mass trends in Greenland in Apr. 2002–Aug. 2023 obtained after a modification of the input dataset or the data processing scheme, as well as the differences with respect to the definitive estimates reported in Table 5

Data processing variant	DS	N	NW	W	SW	SE	NE	RMS	Entire Greenland
All available	Trend estimate	− 28.3	− 64.9	− 37.9	− 43.9	− 76.4	− 19.4		− 270.8
months considered	Difference	0.02	0.1	− 0.05	− 0.1	0.2	− 0.1	0.1	0.06
Low-degree	Trend estimate	− 27.8	− 64.7	− 37.6	− 43.4	− 76.3	− 18.6		− 268.3
SHCs included	Difference	0.5	0.4	0.3	0.3	0.3	0.7	0.5	2.6
Unweighted estimates	Trend estimate	− 27.5	− 64.4	− 36.8	− 40.6	− 80.6	− 20.5		− 270.4
of SHC trends	Difference	0.8	0.7	1.1	3.1	-4.0	− 1.1	2.2	0.5
6378-km	Trend estimate	− 30.3	− 58.8	− 35.0	− 47.2	− 68.8	− 18.7		− 258.9
sphere	Difference	− 2.0	6.2	2.9	− 3.5	7.8	0.6	4.5	12.0
6357-km	Trend estimate	− 28.0	− 65.0	− 37.0	− 46.1	− 77.5	− 19.2		− 272.8
sphere	Difference	0.3	0.008	0.9	− 2.3	− 0.9	0.2	1.1	− 1.9

Units: Gt/yr

adjustment (see Supplementary material II). That example shows that a function can be restored from an incomplete spectrum as accurately as from a complete one, provided that a regularization is used to constrain the inversion results in line with available prior knowledge.

We have also analyzed the effect of refraining from the optimal data weighting in the context of SHC trend estimation. In Sect. 5.5, we have already considered this effect using as input different GRACE/GFO solutions complete to degree 96. We interpreted that effect as a conservative estimate of the bias introduced by optimal data weights when both those weights and the trends themselves are subject to inter-annual variations. Rows 6 and 7 in Table 6 show that this effect stays in most of cases at the level of 1 Gt/yr or lower when the primary dataset is considered. An exception are southern DSs—SW and SE—where this effect reaches 3–4 Gt/yr. This is rather consistent with the findings of Sect. 5.5. Even though the primary dataset shows a somewhat higher sensitivity to the adopted data weighting, its effect also remains within the estimated error limits.

Finally, we have analyzed the effect of refraining from the ellipsoidal Earth approximation in the context of the functional model connecting SHC trends and EWH trends (Eq. A.5). To begin with, let us assume that all the mass variations take place at the sphere of the radius equal to the equatorial radius of the Earth ($\approx$ 6378 km). Rows 8 and 9 in Table 6 show that this assumption results in a noticeable underestimation of the mass losses integrated over most of the DSs. As a result, the mass balance of entire Greenland is also underestimated—by 12 Gt/yr, which exceeds our error margins. We have also considered the sphere of radius equal to the polar Earth's radius ($\approx$ 6357 km), which is close to the radial coordinates of the points at the Earth's surface in Greenland. In that case, the regional mass trends integrated over individual DSs are close to those estimated at the ellipsoidal surface, whereas the mass loss rate of entire Greenland is overestimated by about 2 Gt/yr (see rows 10 and 11 in the aforementioned table). These computations demonstrate that it is important to use properly defined radial coordinates of the points at the Earth's surface when inverting SHC trends into mass trends. Overestimated radial coordinates imply an underestimation of the distances between the Earth's surface and the GRACE satellite orbits. Therefore, the signals sensed by GRACE satellites can be explained by smaller mass changes at the Earth surface. An opposite effect is observed when the radial coordinates of the points at the Earth surface are underestimated. All this suggests that the usage of an ellipsoidal approximation is a must in the context of a *global* estimation of mass anomalies, when radial coordinates of the points at the Earth surface vary by $\approx$ 21 km (even if the terrain is ignored).

Table 7 Comparison of regional mass trends in Greenland obtained in different studies (Gt/yr)

Study and input data	Time interval	N	NW	W	NW+W	SW	SE	NE	Entire Greenland
Wang et al. (2024)	04.2002								
(Tongji L2)	to	$\frac{-23.8}{-28.5}$	$\frac{-58.0}{-65.5}$	$\frac{-38.0}{-38.6}$		$\frac{-38}{-46.3}$	$\frac{-71.5^{**}}{-75.4}$	$\frac{-15.9^{*}}{-20.6}$	$\frac{-252.4}{-274.9}$
vs. this study	09.2022								
Loomis et al. (2021)	04.2002								
(L1b)—ellipsoid	to	$\frac{-25}{-27.9}$	$\frac{-60}{-65.6}$	$\frac{-44}{-39.5}$		$\frac{-61^{**}}{-47.8}$	$\frac{-78^{*}}{-77.8}$	$\frac{-18}{-22.2}$	$\frac{-286}{-280.7}$
vs. this study	09.2020								
Loomis et al. (2021)	04.2002								
(L1b)—6357-km sphere	to	$\frac{-25}{-27.9}$	$\frac{-59}{-65.6}$	$\frac{-43}{-39.5}$		$\frac{-61^{**}}{-47.8}$	$\frac{-77^{*}}{-77.8}$	$\frac{-18}{-22.2}$	$\frac{-282\pm35}{-280.7}$
vs. this study	09.2020								
Velicogna et al. (2020)	04.2002								
(JPL L2)	to	$\frac{-35^{*}}{-27.0}$			$\frac{-91^{**}}{-104.7}$	$\frac{-38}{-46.8}$	$\frac{-89}{-80.5}$	$\frac{-9}{-22.0}$	$\frac{-261\pm45}{-281.0}$
vs. this study	09.2019								

We report the publications from which the trend estimates are taken over, as well as the type of input data exploited in those publications ("L1B" stands for Level-1B data, whereas "L2" stands for Level-2 data, i.e., SHCs). In each case, the result from a previous study is shown as the numerator, and the corresponding result of this study as the denominator. The estimates based on Loomis et al. (2021) are computed by ourselves on the basis of provided EWH trends per mascon, since the original publication reported only the trend integrated over entire Greenland. Two variants of the estimates have been computed: (i) assuming that mass anomalies are located at the surface of the reference ellipsoid and (ii) assuming that mass anomalies are located at the surface of the 6357-km sphere. In the latter case, the mass trend integrated over entire Greenland is consistent with that reported by Loomis et al. (2021) themselves, namely -282 Gt/yr. "Tongji" refers to Tongji-Grace2022 time-series of monthly SHC sets complete to spherical harmonic degree 96. The time interval considered by Wang et al. (2024) is guessed on the basis of the overall context of that publication; the authors themselves repeatedly defined their time interval as "April 2002 to September", whatever that means. The uncertainty ranges reported by Wang et al. (2024) are not taken over, since they were not clearly defined and, most likely, did not account for the effects of signal leakage, as well as GIA uncertainties. Velicogna et al. (2020) used only 5 DS; their northwest DS approximately corresponds to a combination of NW and W DSs in our study, which explains why an additional column "NW+W" is included. A visual inspection of DS geometries revealed that the DSs defined in some other studies may be somewhat smaller or larger than in our study; the corresponding numbers in the table are marked accordingly
*the DS area was somewhat smaller than in this study;
**the DS area was somewhat larger than in this study

6.3 Comparison with the results of other studies

To evaluate the regional mass trends produced with the proposed data processing scheme, we compare them with those reported in recent publications by Wang et al. (2024), Croteau et al. (2021), Loomis et al. (2021), and Velicogna et al. (2020). Since the time intervals considered in those publications are shorter than our primary time interval (Apr. 2002–Aug. 2023), we have applied our data processing scheme to produce a set of alternative trend estimates, using each time only the ITSG monthly solutions in the time interval addressed in a given publication. Importantly, the paper by Loomis et al. (2021) reports the regional mass trend integrated over entire Greenland (as well as over some other areas), but not those integrated over individual DSs within Greenland. Therefore, we have produced the missing numbers ourselves, using the provided EWH trend estimates per mascon. In doing so, we have calculated the mascons areas using two alternative mathematical expressions: (i) with a simple formula for the patch area on a sphere and (ii) with the formula for the patch area on the reference ellipsoid presented in Appendix C. In the former case, the radius of the sphere is set equal to the polar radius of the Earth, i.e., about 6357 km. It turns out that the rate of the total mass loss in Greenland calculated with the former approach perfectly matches the one published by Loomis et al. (2021) themselves (282 Gt/yr). In contrast, the result based on the latter formula exceeds the published one by about 4 Gt/yr. The difference between the two approaches is not surprising, since the area of a surface element near the poles is larger in case of a reference ellipsoid, as compared to the sphere with the radius equal to the polar radius of the Earth.

The results of a comparison with Wang et al. (2024), Loomis et al. (2021), and Velicogna et al. (2020) are presented in Table 7. One can see that the mass losses integrated over individual DSs from Wang et al. (2024) are systematically lower than those in our study. This results in a substantially lower rate of mass loss integrated over entire Greenland: $\approx$ 252 Gt/yr (vs. $\approx$ 275 Gt/yr in our case). A possible reason is a different approach to the choice of the regularization adopted in that publication. Their goal was to produce optimal trend estimates per outlet glacier. As a result, they likely adopted a more aggressive regularization than ours. We remind that we could afford a very weak regularization in the coastal zone because noise at short spatial

scales largely averages out in the course of integration over DSs (to say nothing about entire Greenland).

In contrast, the rate of mass loss in entire Greenland estimated by Loomis et al. (2021) shows an excellent agreement with our estimate: the difference is only 2–5 Gt/yr (depending on what formula for the mascon area is used). The mass loss integrated over individual DSs shows a reasonable agreements: the differences stay at the level of a few Gt/yr. The largest mismatch ($\approx$ 13 Gt/yr) is observed for SW DS, which might be due to a difference in the DS geometry.

The mass loss rates per DS reported by Velicogna et al. (2020) also show a reasonable agreement with ours, even though their numbers are based on EWH trends estimates of a rather low spatial resolution (cf. Fig.2e in their publication). The differences do not exceed 14 Gt/yr. Their rate of total mass loss in Greenland is less than ours by 20 Gt/yr, which is still within the error limits reported by Velicogna et al. (2020): $\pm$45 Gt/yr.

A comparison with Croteau et al. (2021) is limited to the mass trend integrated over entire Greenland, since these authors did not report similar estimates for individual DSs. They found that the rate of mass loss in Greenland in 04.2002–04.2021 was 274 $\pm$ 13 Gt/yr. This is slightly less than our estimate—279.2 Gt/yr, though the difference is within the error margins.

7 Discussion

Our study shows how GRACE/GFO-based SHCs can be used to obtain accurate estimates of regional mass anomalies for target areas (in our case, Greenland's DSs, as well as Greenland as a whole). Key elements of our approach are: (i) direct inversion of SHCs (or SHC trends) into a global distribution of mass anomalies in terms of EWH (or their trends); (ii) spatially-varying first-order Tikhonov regularization that takes into account available information about the behavior of mass anomalies; and (iii) rigorous optimization of the data processing scheme consistently with the target estimates.

Direct inversion of SHCs into a global set of mass anomalies does not suffer from the introduction of intermediate quantities, such as gravity disturbances at the satellite altitude, which is a must in a regional data inversion (e.g., Forsberg and Reeh 2007; Baur and Sneeuw 2011; Ran et al. 2018a). This not only makes the data inversion easier from the conceptual point of view, but also simplifies the usage of available stochastic information about the accuracy of SHCs. Furthermore, recovery of mass anomalies *globally*, even if the target region is limited, allows one to mitigate the impact of mass re-distribution outside the target region without using additional models (e.g., hydrological models).

Available information about the spatial behavior of mass anomalies is very important prior knowledge, the value of which is frequently underestimated in GRACE data processing. GRACE/GFO data lack information about short spatial scales (i.e., high spherical harmonic degrees), so that it is necessary to use prior knowledge to bridge this gap. Our experience tells that an attempt to introduce prior knowledge as a formal mathematical constraint (like a requirement that the solution norm must be minimal) yields solutions that are similar to those obtained with the spherical harmonic synthesis. In view of the Parceval's identity, this is not surprising: the minimum norm in the spatial domain corresponds to the minimal sum of SHCs squared in the frequency domain. Therefore, the resulting estimates lack high-frequency signal if the data do not contain high-frequency information. However, results of the spherical harmonic synthesis suffer from significant ringing artifacts if the actual mass anomalies are characterized by abrupt changes in the spatial domain (see, e.g., the left panel in Fig. 2). In contrast, physical constraints based on available information about mass anomalies may introduce high-frequency information which is absent in the data. In Greenland, for instance, this is the knowledge that mass anomalies in the central part are subject to only minor spatial variations. This allows the ringing artefact there to be mitigated. Thus, the recovered mass anomalies are to be limited to a narrow coastal zone, which makes them much more realistic.

In addition, we find it critical to maintain consistency between the data processing optimization criterion on the one hand and the target regions and time intervals on the other hand, since this allows the information content of data to be fully exploited. In recovery of mass anomalies integrated over DSs, for instance, this allows for a very small regularization in the coastal zone. The resulting increase in the noise level is mitigated by averaging the recovered mass anomalies over the entire DSc. Importance of a proper choice of the data processing optimization is frequently underestimated. For instance, it seems to be natural to optimize (explicitly or implicitly) the data processing for the best recovery of mass anomalies in the point-wise sense. However, this results in a rather aggressive filtering or regularization (depending on what approach is used to cope with data noise). As a consequence, the recovered signals are subject to an excessive damping, when mass anomalies integrated over large regions are of interest. Most probably, this is the reason why many alternative estimates of regional mass losses in Greenland, which are addressed in Sect. 6.3, are smaller than our estimates. This is in line with our statement in the introductory section that the usage of off-the-shelf data products is frequently is a sub-optimal choice.

We have also demonstrated that random noise in GRACE data provides only a minor contribution to the noise budget of regional mass trend estimates in our case. This is consistent with only a minor difference between trend estimates based on GRACE/GFO data products from different data process-

ing teams (see Table 4). This means that one can substantially reduce the amount of input data without a substantial deterioration of SNR (assuming the current level of other errors). For instance, equally accurate mass trend estimates are likely achievable not only on the basis of 20+ years of data, but also over much shorter time intervals. Alternatively, an accurate estimation of regional mass trends integrated over smaller areas than the considered DSs is likely achievable in this way—both in Greenland and in other regions.

One may ask: what is the smallest distance between the areas where mass trends can be reliably separated from each other? The answer is quite simple: since the maximum spherical harmonic degree of the exploited monthly solutions is $L_{\max} = 120$, the maximal achievable spatial resolution in terms of half-wavelengths is $20{,}000/L_{\max} \approx 167$ km (see, e.g., Pail et al. 2011). This is the resolution we expected to have in the coastal zone, where the regularization is the smallest. To check if this is indeed the case, we perform a "chessboard test". In that test, the coastal zone is tiled with patches of the size 1.6° (North-South direction) times 4° (East-West direction). In the southern part of Greenland, the size of those patches is close to the theoretically achievable spatial resolution or slightly larger (at the 70°N latitude, for instance, the size is 178 × 153 km). A plus-minus unit mass anomaly is assigned to each of these patches chequerwise (see Supplementary Fig. S.4a). Noteworthy, a small mass anomaly is assigned to the entire ocean area in order to ensure a global mass conservation (that is, the total mass anomaly integrated world-wide is zero). This pattern is converted into a set of SHCs up to $L_{\max} = 120$. The computed SHCs are inverted into a global set of mass anomalies using the same optimized data inversion scheme, as was applied to real GRACE/GFO data. The resulting mass anomaly distribution demonstrates that mass anomalies associated with individual patches are indeed distinguishable in the southern Greenland (Fig. S.4b). This is not the case, however, in the northern part (starting from approximately 74°N latitude). This is not surprising, since the East-West size of the patches there is too small. In order to make a fair resolution analysis of the northern part of Greenland, we make a similar test, having increased the East-West size of the patches to 10° (Fig. S.4c). At the 81.2°N latitude, for instance, the size of new patches is 179 × 171 km. The mass anomaly pattern recovered in this case demonstrates that the achievable spatial resolution is close to the theoretical limit also in the northern part of Greenland (Fig. S.4d).

Finally, we have shown that signal leakage and uncertainties of GIA modelling may affect the estimates of regional mass trends in Greenland much more substantially than random errors. At the same time, it is not unlikely that the role of the latter will be larger when different scenarios are considered (e.g., if regional mass trends are estimated over much shorter time intervals). All this implies that more efforts are needed to develop GRACE/GFO data processing further. This may include: (i) development of a more advanced data weighting scheme to derive long-term trends (or/and other regular signals) in the presence of inter-annual variations in both errors and signals; (ii) usage of an advanced Earth System Model (Dobslaw et al. 2015) instead of altimetry-based elevation trends to synthesize more realistic signals for numerical experiments; (iii) usage of more comprehensive stochastic models of errors in the exploited GRACE/GFO monthly solutions (including the usage of full error variance-covariance matrices); (iv) development of more advanced regularization schemes; and (v) more accurate estimation of GIA uncertainties, taking into account alternative estimates of GIA signal in Greenland (see, e.g., Simpson et al. 2011; Lecavalier et al. 2014). All this may allow both for a better optimization of data processing and for a less conservative estimation of contributors to the noise budget.

8 Conclusions

Advanced data processing has been developed for a precise estimation of mass anomalies integrated over given target regions from level-2 GRACE/GFO data. It is based on a direct regularized inversion of SHCs (or SHC trends) into a global distribution of mass anomalies in terms of EWH (or their trends). In contrast to various data processing schemes based on spherical harmonic synthesis, the developed methodology does not require the knowledge of all the SHCs up to a certain maximum degree. It is shown, for instance, that the omission of degree-1, $C_{2,0}$, and $C_{3,0}$ coefficients does not deteriorate the obtained results.

The developed methodology has been applied to estimate the mass balance of the entire GrIS, as well as its individual DSs in Apr. 2002–Aug. 2023. It is shown that the regional mass loss rates in Greenland's DSs varied between 19 ± 4 Gt/yr (northeast DS) and 77±7 Gt/yr (southeast DS). The rate of the total mass loss in Greenland is estimated as 271 ± 10 Gt/yr.

It is demonstrated that the mass balance estimates are rather sensitive to the time interval under consideration. For instance, a reduction of this interval by about 3 years (to Apr.2002–Sep.2020) increases the total rate of mass loss in Greenland by 10 Gt/yr (to 281 Gt/yr). As such, the obtained estimates are in a good agreement with those of Loomis et al. (2021), who reported the total mass loss rate of 282±35 Gt/yr in the same time interval. At the same time, this implies that one should use off-the-shelf high-resolution trend estimates, like those of Loomis et al. (2021), with a caution: they may not be applicable to time intervals deviating from the one adopted originally.

It is also shown that the spherical Earth assumption should not be applied in the context of precise estimates of mass

anomalies, especially if global estimates are of interest. For instance, the assumption that the Earth is a sphere of $\approx 6,378$ km radius reduces the rate of total mass loss in Greenland by 12 Gt/yr (which exceeds the error limits of the estimate). Most probably, this is because the assumed distance between the GrIS surface and the satellite orbits is reduced in this case by ≈ 20 km, so that weaker mass losses are sufficient to explain the signals sensed by GRACE/GFO satellites.

The developed data processing methodology allows, among other, for a rather accurate estimation of mass balance of individual DSs in Greenland (in average, the estimated error is below 5 Gt/yr). As a consequence, the obtained estimates are characterized by sufficiently high SNR: between 5 in the northeast DS and 42 in the northwest DS. This opens the door, among other, for using GRACE/GFO data for a comparison, validation, and calibration of physical models describing mass changes in Greenland, including its SMB, at the scale of individual DSs. A comprehensive analysis of those models on the basis of the obtained GRACE/GFO-based mass balance estimates will be the subject of a separate publication.

Appendix A. Relationship between mass anomalies at the surface of the reference ellipsoid and SHC variations

The relationship between 3-D density variations $\Delta\rho$ in the Earth system and SHC variations $\Delta\bar{C}_{lm}$ can be represented as follows (Wahr et al. 1998):

$$\Delta\bar{C}_{lm} = \frac{1}{M_E\,(2l+1)} \iiint_{v} \Delta\rho\,(r,\theta,\phi)\left(\frac{r}{a}\right)^{l} \bar{Y}_{lm}(\theta,\phi)\,\mathrm{d}v, \tag{A.1}$$

where l and m are the spherical harmonic degree and order, respectively (we assume that the order runs from $-l$ to l, so that positive orders correspond to cosinusoidal spherical harmonics and negative orders to sinusoidal ones); M_E is the Earth's mass; a is the Earth's equatorial radius; $\bar{Y}_{lm}(\theta,\phi)$ are 4π-normalized surface spherical harmonics:

$$\bar{Y}_{lm}(\theta,\phi) = \bar{P}_{l,|m|}(\cos\theta)\begin{cases}\cos m\phi & (m \geq 0)\\ \sin(-m\phi) & (m < 0)\end{cases} \tag{A.2}$$

with $\bar{P}_{l,m}$ being normalized associated Legendre functions; r, θ and ϕ are geocentric coordinates of the current point (i.e., radial coordinate, co-latitude, and longitude, respectively); v is the 3-D domain covering the entire Earth system; and $\mathrm{d}v$ is a volume element.

Let us assume that all the density variations occur only in a thin layer located at the surface of the reference ellipsoid, i.e., in the layer limited by radial coordinates $r(\theta)$ and $r(\theta)+\varepsilon$, where function $r(\theta)$ describes the surface of the reference ellipsoid and ε is an infinitesimal value. Then, these density variations can be represented in terms of Equivalent Water Heights (EWH) h_w:

$$h_w(\theta,\phi) = \frac{1}{\rho_w}\int_{r(\theta)}^{r(\theta)+\varepsilon} \Delta\rho(r,\theta,\phi)\,\mathrm{d}r, \tag{A.3}$$

where ρ_w is water density. Notice that we approximate the integration along the ellipsoidal normal with the integration along the radial coordinate. The relative error introduced by this approximation does not exceed 10^{-5}, which is believed to be tolerable.

Taking Eq. (A.3) into account, we can re-write Eq. (A.1) as follows:

$$\begin{aligned}\Delta\bar{C}_{lm} &= \frac{1}{M_E(2l+1)} \iint_{\Omega}\int_{r(\theta)}^{r(\theta)+\varepsilon} \\ &\quad \Delta\rho(r,\theta,\phi)\left(\frac{r}{a}\right)^{l}\bar{Y}_{lm}(\theta,\phi)\mathrm{d}r\,\mathrm{d}\Omega \\ &= \frac{\rho_w}{M_E(2l+1)} \iint_{\Omega} h_w(\theta,\phi)\left(\frac{r(\theta)}{a}\right)^{l}\bar{Y}_{lm}(\theta,\phi)\,\mathrm{d}\Omega,\end{aligned} \tag{A.4}$$

where Ω is the surface of the reference ellipsoid and $d\Omega$ is an element of that surface.

Equation (A.4) describes the direct relationship between mass anomalies at the surface of the reference ellipsoid and SHC variations. However, this relationship does not take into account that the Earth is an elastic body, so that mass re-distribution at its surface results in its deformations, which, in turn, also affect SHC variations. To take the latter effect into account, we introduce corrections based on load Love numbers k_l (Wahr et al. 1998). Thus, the final expression for the relationship between mass anomalies and SHC variations is:

$$\Delta\bar{C}_{lm} = \frac{\rho_w(1+k_l)}{M_E(2l+1)} \iint_{\Omega} h_w(\theta,\phi)\left(\frac{r(\theta)}{a}\right)^{l}\bar{Y}_{lm}(\theta,\phi)\,\mathrm{d}\Omega. \tag{A.5}$$

Noteworthy, the integration in Eq. (A.5) can be performed either in geocentric or in geographic coordinates. We prefer the latter option, since it allows the inversion results to be used as they are. This requires, however, that geographic coordinates are converted into geocentric ones when the values of surface spherical harmonics at a given point are computed.

This conversion, as well as the computation of radial coordinates $r(\theta)$, can be easily performed via the computation of Cartesian coordinates of a given point as an intermediate product.

Appendix B. Integration of a function over a rectangular cell at the surface of an ellipsoid of rotation

Let us consider the integration of a given function of geodetic coordinates $f(\theta, \phi)$ over an area ω at the surface of an ellipsoid of rotation:

$$J = \iint\limits_{\omega} f(\theta, \phi)\, \mathrm{d}\omega. \tag{B.1}$$

Let ω be a rectangular area with the northern, southern, western, and eastern boundary equal to θ_1, θ_2, ϕ_1, and ϕ_2, respectively. The integration prescribed by Eq. (B.1) can be split into integration over longitudes and integration over co-latitudes. The former integration yields:

$$I(\theta) = p(\theta) \int\limits_{\phi_1}^{\phi_2} f(\theta, \phi)\, \mathrm{d}\phi \tag{B.2}$$

with $p(\theta)$ being the radius of the parallel at co-latitude θ:

$$p(\theta) = N(\theta) \sin\theta, \tag{B.3}$$

where $N(\theta)$ is the so-called "transverse radius of curvature":

$$N(\theta) = \frac{a^2}{\sqrt{(a\sin\theta)^2 + (b\cos\theta)^2}} = \frac{a}{\sqrt{1 - e^2 cos^2\theta}}; \tag{B.4}$$

in this expression, a and b are the ellipsoid's semi-major and semi-minor axis, respectively, and e is its eccentricity:

$$e = \sqrt{1 - \frac{b^2}{a^2}}. \tag{B.5}$$

Next, the integration over the region within an infinitesimal co-latitude band $\mathrm{d}\theta$ can be written as:

$$\mathrm{d}J(\theta) = I(\theta)\, \mathrm{d}L, \tag{B.6}$$

where $\mathrm{d}L$ is the length of meridional arc within co-latitude band $\mathrm{d}\theta$:

$$\mathrm{d}L = M(\theta)\, \mathrm{d}\theta \tag{B.7}$$

with

$$M(\theta) = \frac{\partial L}{\partial \theta}; \tag{B.8}$$

this quantity is called "meridional radius of curvature" and equal to:

$$M(\theta) = \frac{(ab)^2}{\left[(a\sin\theta)^2 + (b\cos\theta)^2\right]^{\frac{3}{2}}} = \frac{1 - e^2}{a^2} N^3(\theta). \tag{B.9}$$

Substitution of Eq. (B.7) into Eq. (B.6) allows the integration over co-latitudes to be written as follows:

$$J = \int\limits_{\theta_1}^{\theta_2} I(\theta) M(\theta)\, \mathrm{d}\theta. \tag{B.10}$$

Taking into account Eq. (B.2), we find that the integration of function $f(\theta, \phi)$ over the entire cell can be implemented with the following expression:

$$J = \int\limits_{\theta_1}^{\theta_2} N(\theta) M(\theta) \sin\theta \left(\int\limits_{\phi_1}^{\phi_2} f(\theta, \phi)\, \mathrm{d}\phi \right) \mathrm{d}\theta. \tag{B.11}$$

In view of Eqs. (B.9) and (B.4), this expression can also be written as

$$\begin{aligned} J &= \frac{1 - e^2}{a^2} \int\limits_{\theta_1}^{\theta_2} N^4(\theta) \sin\theta \left(\int\limits_{\phi_1}^{\phi_2} f(\theta, \phi)\, \mathrm{d}\phi \right) \mathrm{d}\theta \\ &= a^2(1 - e^2) \int\limits_{\theta_1}^{\theta_2} \frac{\sin\theta}{(1 - e^2\, \cos^2\theta)^2} \\ &\quad \left(\int\limits_{\phi_1}^{\phi_2} f(\theta, \phi)\, \mathrm{d}\phi \right) \mathrm{d}\theta. \end{aligned} \tag{B.12}$$

Furthermore, it follows from Eq. (B.5) that

$$1 - e^2 = \frac{b^2}{a^2}. \tag{B.13}$$

Then, we finally have:

$$J = b^2 \int\limits_{\theta_1}^{\theta_2} \frac{\sin\theta}{(1 - e^2\, \cos^2\theta)^2} \left(\int\limits_{\phi_1}^{\phi_2} f(\theta, \phi)\, \mathrm{d}\phi \right) \mathrm{d}\theta. \tag{B.14}$$

If the function to be integrated does not depend on longitude, this expression simplifies to:

$$J = (\phi_2 - \phi_1)\, b^2 \int_{\theta_1}^{\theta_2} \frac{f(\theta)\, \sin\theta}{(1 - e^2\, \cos^2\theta)^2}\, \mathrm{d}\theta. \tag{B.15}$$

Appendix C: Area of an element at the surface of an ellipsoid of rotation

Let us apply Eq. (B.15), having set $f(\theta) = 1$. Then, that expression allows the area S of a surface element to be expressed as:

$$S = (\phi_2 - \phi_1)\, b^2 \int_{\theta_1}^{\theta_2} \frac{\sin\theta}{(1 - e^2\, \cos^2\theta)^2}\, \mathrm{d}\theta. \tag{C.1}$$

A substitution $t = \cos\theta$ allows the integral in the latter expression to be re-written as follows:

$$\begin{aligned}
&\int_{\theta_1}^{\theta_2} \frac{\sin\theta}{(1 - e^2\, \cos^2\theta)^2}\, \mathrm{d}\theta \\
&= \int_{\cos\theta_2}^{\cos\theta_1} \frac{1}{\left(1 - e^2\, t^2\right)^2}\, \mathrm{d}t = e^{-4} \int_{\cos\theta_2}^{\cos\theta_1} \frac{1}{\left(t^2 - e^{-2}\right)^2}\, \mathrm{d}t \\
&= e^{-4} \left[\frac{-t}{2e^{-2}(t^2 - e^{-2})} + \frac{1}{4e^{-3}} \log \left| \frac{t + e^{-1}}{t - e^{-1}} \right| \right] \Bigg|_{t=\cos\theta_2}^{t=\cos\theta_1} \\
&= \frac{1}{2} \left(\frac{\cos\theta_1}{1 - e^2 \cos^2\theta_1} - \frac{\cos\theta_2}{1 - e^2 \cos^2\theta_2} \right) \\
&\quad + \frac{1}{4e} \log \left(\frac{1 + e\cos\theta_1}{1 - e\cos\theta_1} \cdot \frac{1 - e\cos\theta_2}{1 + e\cos\theta_2} \right).
\end{aligned} \tag{C.2}$$

By combining this expression with Eq. (C.1), we readily obtain:

$$\begin{aligned}
S = (\phi_2 - \phi_1)\, b^2 \Bigg[&\frac{1}{2} \left(\frac{\cos\theta_1}{1 - e^2 \cos^2\theta_1} - \frac{\cos\theta_2}{1 - e^2 \cos^2\theta_2} \right) \\
&+ \frac{1}{4e} \log \left(\frac{1 + e\cos\theta_1}{1 - e\cos\theta_1} \cdot \frac{1 - e\cos\theta_2}{1 + e\cos\theta_2} \right) \Bigg].
\end{aligned} \tag{C.3}$$

Supplementary Information The online version contains supplementary material available at https://doi.org/10.1007/s00190-025-02028-3.

Acknowledgements The author thanks Roland Klees, Weiran Li, handling editor Frank Lemoine, and four anonymous reviewers for numerous valuable comments, which facilitated a substantial improvement of the manuscript. Generic Mapping Tools (GMT) software (Wessel et al. 2013) was used to create all the plots.

Author Contributions The entire research was conducted by the single author.

Data Availability The time-series of monthly GRACE and GFO solutions exploited in this study were downloaded from the International Centre for Global Earth Models (http://icgem.gfz-potsdam.de/series; ftp://isdcftp.gfz-potsdam.de). The altimetry-based trends in surface elevation in Greenland are distributed within the frame of the ESA Climate Change Initiative (ESA-CCI; http://products.esa-icesheets-cci.org). To model GIA signal, we used the ICE-6G model, having chosen the variant of Stokes coefficients obtained with a higher resolution calculation (https://www.atmosp.physics.utoronto.ca/~peltier/data.php, file *ICE-6G_High_Res_Stokes_trend.txt.gz*).

References

Baur O, Sneeuw N (2011) Assessing Greenland ice mass loss by means of point-mass modeling: a viable methodology. J Geod 85:607–615. https://doi.org/10.1007/s00190-011-0463-1

Bettadpur SV (2018) GRACE 327-742 (CSR-GR-12-xx), Gravity Recovery and Climate Experiment, UTCSR Level-2 Processing Standards Document (Rev 5.0 Apr 18, 2018) (For Level-2 Product Release 0006). Center for Space Research, University of Texas at Austin

Bonin J, Chambers D (2013) Uncertainty estimates of a GRACE inversion modelling technique over Greenland using a simulation. Geophys J Int 194(1):212–229. https://doi.org/10.1093/gji/ggt091

Cazenave A, Dominh K, Guinehut S, Berthier E, Ramillien WLG, Ablain M, Larnicol G (2009) Sea level budget over 2003–2008: A reevaluation from GRACE space gravimetry, satellite altimetry and Argo. Glob Planet Change 65:83–88. https://doi.org/10.1016/j.gloplacha.2008.10.004

Chang G, Qian N, Bian S (2023) Statistically optimal estimation of surface mass anomalies by directly using GRACE level-2 spherical harmonic coefficients as measurements. Geophys J Int 233(3):1786–1799. https://doi.org/10.1093/gji/ggad024

Cheng M, Tapley BD, Ries JC (2013) Deceleration in the Earth's oblateness. J Geophys Res Solid Earth 118(2):740–747. https://doi.org/10.1002/jgrb.50058

Cirací E, Velicogna I, Swenson S (2020) Continuity of the mass loss of the World's glaciers and ice caps from the GRACE and GRACE Follow-On missions. Geophys Res Lett 47(9). https://doi.org/10.1029/2019GL086926

Croteau M, Sabaka T, Loomis B (2021) GRACE fast mascons from spherical harmonics and a regularization design trade study. J Geophys Res Solid Earth 126(8). https://doi.org/10.1029/2021JB022113

Dahle C, Flechtner F, Murböck M, Michalak G, Neumayer H, Abrykosov O, Reinhold A, König R (2018) GRACE 327-743 (Gravity Recovery and Climate Experiment), GFZ Level-2 Pro-

cessing Standards Document for Level-2 Product Release 06 (Rev. 1.0, October 26, 2018), (Scientific Technical Report STR - Data; 18/04). Potsdam: GFZ German Research Centre for Geosciences, https://doi.org/10.2312/GFZ.b103-18048

Daras I, March G, Pail R, Hughes CW, Braitenberg C, Güntner A, Eicker A, Wouters B, Heller-Kaikov B, Pivetta T, Pastorutti A (2024) Mass-change And Geosciences International Constellation (MAGIC) expected impact on science and applications. Geophys J Int 236:1288–1308. https://doi.org/10.1093/gji/ggad472

Ditmar P (2018) Conversion of time-varying Stokes coefficients into mass anomalies at the Earth's surface considering the Earth's oblateness. J Geod 92:1401–1412. https://doi.org/10.1007/s00190-018-1128-0

Ditmar P (2022) How to quantify the accuracy of mass anomaly time-series based on GRACE data in the absence of knowledge about true signal? J Geod 96, article number 54. https://doi.org/10.1007/s00190-022-01640-x

Ditmar P, Kusche J, Klees R (2003) Computation of spherical harmonic coefficients from gravity gradiometry data to be acquired by the GOCE satellite: regularization issues. J Geod 77:465–477. https://doi.org/10.1007/s00190-003-0349-y

Dobslaw H, Bergmann-Wolf I, Dill R, Forootan E, Klemann V, Kusche J, Sasgen I (2015) The updated ESA Earth System Model for future gravity mission simulation studies. J Geod 89(5):505–513. https://doi.org/10.1007/s00190-014-0787-8

Ewert H, Groh A, Dietrich R (2012) Volume and mass changes of the Greenland ice sheet inferred from ICESat and GRACE. J Geodyn 59–60:111–123. https://doi.org/10.1016/j.jog.2011.06.003

Forsberg R, Reeh N (2007) Mass change of the Greenland ice sheet from GRACE. In: Proceedings of the 1st Int. Symp. of IGFS, Harita Dergisi, Vol 18, pp 454–458

Forsberg R, Sørensen L, Simonsen S (2017) Greenland and Antarctica Ice Sheet mass changes and effects on global sea level. Surv Geophys 38(1):89–104. https://doi.org/10.1007/s10712-016-9398-7

Frappart F, Ramillien G (2018) Monitoring groundwater storage changes using the Gravity Recovery and Climate Experiment (GRACE) satellite mission: A review. Remote Sens 10(6), Article number 829. https://doi.org/10.3390/rs10060829

Güntner A (2008) Improvement of global hydrological models using GRACE data. Surv Geophys 29(4–5):375–397. https://doi.org/10.1007/s10712-008-9038-y

Han SC, Shum C, Matsumoto K (2005) GRACE observations of M_2 and S_2 ocean tides underneath the Filchner-Ronne and Larsen ice shelves, Antarctica. Geophys Res Lett 32(20):1–5, Article number L20311. https://doi.org/10.1029/2005GL024296

Han SC, Shum CK, Bevis M, Ji C, Kuo CY (2006) Crustal dilatation observed by GRACE after the 2004 Sumatra-Andaman earthquake. Science 313:658–662. https://doi.org/10.1126/science.1128661

Heiskanen WA, Moritz H (1984) Physical Geodesy. Institute of Physical Geodesy, Technical University Graz, Austria

Hestenes MR, Stiefel E (1952) Methods of conjugate gradients for solving linear systems. J Res Natl Bur Stand 49:409–436

Klees R, Revtova EA, Gunter B, Ditmar P, Oudman E, Winsemius HC, Savanije HH (2008) The design of an optimal filter for monthly GRACE gravity field models. Geophys J Int 175:417–432. https://doi.org/10.1111/j.1365-246X.2008.03922.x

Kusche J (2007) Approximate decorrelation and non-isotropic smoothing of time-variable GRACE-type gravity field models. J Geod 81:733–749. https://doi.org/10.1007/s00190-007-0143-3

Kvas A, Behzadpour S, Ellmer M, Klinger B, Strasser S, Zehentner N, Mayer-Gürr T (2019) ITSG-Grace2018: Overview and evaluation of a new GRACE-only gravity field time series. J Geophys Res Solid Earth 124. https://doi.org/10.1029/2019JB017415

Landerer FW, Wiese DN, Bentel K, Boening C, Watkins MM (2015) North Atlantic meridional overturning circulation variations from GRACE ocean bottom pressure anomalies. Geophys Res Lett 42:8114–8121. https://doi.org/10.1002/2015GL065730

Landerer FW, Flechtner FM, Save H, Webb FH, Bandikova T, Bertiger WI, Bettadpur SV, Byun SH, Dahle C, Dobslaw H, Fahnestock E, Harvey N, Kang Z, Kruizinga GLH, Loomis BD, McCullough C, Murböck M, Nagel P, Paik M, Pie N, Poole S, Strekalov D, Tamisiea ME, Wang F, Watkins MM, Wen HY, Wiese DN, Yuan DN (2020) Extending the global mass change data record: GRACE Follow-On instrument and science data performance. Geophys Res Lett 47(12), https://doi.org/10.1029/2020GL088306

Lecavalier BS, Milne GA, Simpson MJ, Wake L, Huybrechts P, Tarasov L, Kjeldsen KK, Funder S, Long AJ, Woodroffe S, Dyke AS, Larsen NK (2014) A model of Greenland ice sheet deglaciation constrained by observations of relative sea level and ice extent. Quat Sci Rev 102:54–84. https://doi.org/10.1016/j.quascirev.2014.07.018

Loomis BD, Luthcke SB, Sabaka TJ (2019) Regularization and error characterization of grace mascons. J Geod 93(9):1381–1398. https://doi.org/10.1007/s00190-019-01252-y

Loomis BD, Rachlin KE, Wiese DN, Landerer FW, Luthcke SB (2020) Replacing GRACE/GRACE-FO C_{30} with satellite laser ranging: Impacts on Antarctic Ice Sheet mass change. Geophys Res Lett 47(3). https://doi.org/10.1029/2019GL085488

Loomis BD, Felikson D, Sabaka TJ, Medley B (2021) High-spatial-resolution mass rates from GRACE and GRACE-FO: Global and ice sheet analyses. J Geophys Res Solid Earth 126(12). https://doi.org/10.1029/2021JB023024

Luthcke S, Sabaka T, Loomis B, Arendt A, McCarthy J, Camp J (2013) Antarctica, Greenland and Gulf of Alaska land-ice evolution from an iterated GRACE global mascon solution. Journal Glaciol 59(216):613–631. https://doi.org/10.3189/2013JoG12J147

Luthcke SB, Zwally HJ, Abdalati W, Rowlands DD, Ray RD, Nerem RS, Lemoine FG, McCarthy JJ, Chinn DS (2006) Recent Greenland ice mass loss by drainage system from satellite gravity observations. Science 314(5803):1286–1289

Meyssignac B, Boyer T, Zhao Z, Hakuba MZ, Landerer FW, Stammer D, Köhl A, Kato S, L'Ecuyer T, Ablain M, Abraham JP, Blazquez A, Cazenave A, Church JA, Cowley R, Cheng L, Domingues CM, Giglio D, Gouretski V, Ishii M, Johnson GC, Killick RE, Legler D, Llovel W, Lyman J, , Palmer MD, Piotrowicz S, Purkey SG, Roemmich D, Roca R, Savita A, von Schuckmann K, Speich S, Stephens G, Wang G, Wijffels SE, Zilberman N (2019) Measuring global ocean heat content to estimate the Earth energy imbalance. Frontiers in Marine Science 6, article 432. https://doi.org/10.3389/fmars.2019.00432

Noël B, van de Berg WJ, MacHguth H, Lhermitte S, Howat I, Fettweis X, van den Broeke MR (2016) A daily, 1 km resolution data set of downscaled Greenland ice sheet surface mass balance (1958–2015). Cryosphere 10(5):2361–2377. https://doi.org/10.5194/tc-10-2361-2016

Otosaka IN, Shepherd A, Ivins ER, Schlegel NJ, Amory C, van den Broeke M, Horwath M, Joughin I, King M, Krinner G, Nowicki S, Payne T, Rignot E, Scambos T, Simon KM, Smith B, Sandberg Sørensen L, Velicogna I, Whitehouse P, A G, Agosta C, Ahlstrøm AP, Blazquez A, Colgan W, Engdahl M, Fettweis X, Forsberg R, Gallée H, Gardner A, Gilbert L, Gourmelen N, Groh A, Gunter BC, Harig C, Helm V, Khan SA, Konrad H, Langen P, Lecavalier B, Liang CC, Loomis B, McMillan M, Melini D, Mernild SH, Mottram R, Mouginot J, Nilsson J, Noël B, Pattle ME, Peltier WR, Pie N, Sasgen I, Save H, Seo KW, Scheuchl B, Schrama E, Schröder L, Simonsen SB, Slater T, Spada G, Sutterley T, Vishwakarma BD, van Wessem JM, Wiese D, van der Wal W, Wouters B (2023) Mass balance of the Greenland and Antarctic ice sheets from 1992 to 2020. Earth Syst Sci Data 15:1597–1616. https://doi.org/10.5194/essd-15-1597-2023

Pail R, Bruinsma S, Migliaccio F, Förste C, Goiginger H, Schuh WD, Höck E, Reguzzoni M, Brockmann JM, Abrikosov O, Veicherts M, Fecher T, Mayrhofer R, Krasbutter I, Sansò F, Tscherning CC (2011) First GOCE gravity field models derived by three different approaches. J Geod 85(11):819–843. https://doi.org/10.1007/s00190-011-0467-x

Paulson A, Zhong S, Wahr J (2007) Inference of mantle viscosity from grace and relative sea level data. Geophys J Int 171:497–508. https://doi.org/10.1111/j.1365-246X.2007.03556.x

Peralta-Ferriz C, Morison JH, Wallace JM, Bonin JA, Zhang J (2014) Arctic ocean circulation patterns revealed by GRACE. J Clim 27:1445–1468. https://doi.org/10.1175/JCLI-D-13-00013.1

Ran J, Ditmar P, Klees R, Farahani HH (2018) Statistically optimal estimation of Greenland Ice Sheet mass variations from GRACE monthly solutions using an improved mascon approach. J Geod 92:299–319. https://doi.org/10.1007/s00190-017-1063-5

Ran J, Vizcaino M, Ditmar P, van den Broeke MR, Moon T, Steger CR, Enderlin EM, Wouters B, Noël B, Reijmer CH, Klees R, Zhong M, Liu L, Fettweis X (2018) Seasonal mass variations show timing and magnitude of meltwater storage in the Greenland Ice Sheet. Cryosphere 12:2981–2999. https://doi.org/10.5194/tc-12-2981-2018

Rignot E, Velicogna I, van den Broeke MR, Monaghan A, Lenaerts J (2011) Acceleration of the contribution of the Greenland and Antarctic ice sheets to sea level rise. Geophys Res Lett 38(5):L05503. https://doi.org/10.1029/2011GL046583

Rodell M, Famiglietti JS, Wiese DN, Reager JT, Beaudoing HK, Landerer FW, Lo MH (2018) Emerging trends in global freshwater availability. Nature 557:651–659. https://doi.org/10.1038/s41586-018-0123-1

Sasgen I, Martinec Z, Fleming K (2006) Wiener optimal filtering of GRACE data. Stud Geophys Geod 50:499–508. https://doi.org/10.1007/s11200-006-0031-y

Sellevold R, Vizcaino M (2020) Global warming threshold and mechanisms for accelerated Greenland ice sheet surface mass loss. J Adv Model Earth Syst 12(9). https://doi.org/10.1029/2019MS002029

Siemes C, Ditmar P, Riva REM, Slobbe DC, Liu XL, Farahani HH (2013) Estimation of mass change trends in the Earth's system on the basis of GRACE satellite data, with application to Greenland. J Geod 87:69–87. https://doi.org/10.1007/s00190-012-0580-5

Simonsen SB, Sørensen LS (2017) Implications of changing scattering properties on Greenland ice sheet volume change from Cryosat-2 altimetry. Remote Sens Environ 190:207–216. https://doi.org/10.1016/j.rse.2016.12.012

Simpson MJ, Wake L, Milne GA, Huybrechts P (2011) The influence of decadal- to millennial-scale ice mass changes on present-day vertical land motion in Greenland: Implications for the interpretation of GPS observations. J Geophys Res Solid Earth 116(2). https://doi.org/10.1029/2010JB007776

Sørensen LS, Simonsen SB, Forsberg R, Khvorostovsky K, Meister R, Engdahl ME (2018) 25 years of elevation changes of the Greenland Ice Sheet from ERS, Envisat, and CryoSat-2 radar altimetry. Earth Planet Sci Lett 495:234–241. https://doi.org/10.1016/j.epsl.2018.05.015

Stuhne GR, Peltier WR (2015) Reconciling the ICE-6G_C reconstruction of glacial chronology with ice sheet dynamics: The cases of Greenland and Antarctica. J Geophys Res Earth Surf 120:1–25. https://doi.org/10.1002/2015JF003580

Sun Y, Riva R, Ditmar P (2016) Optimizing estimates of annual variations and trends in geocenter motion and J_2 from a combination of GRACE data and geophysical models. J Geophys Res Solid Earth 121(11):8352–8370. https://doi.org/10.1002/2016JB013073

Sun Y, Ditmar P, Riva R (2017) Statistically optimal estimation of degree-1 and C_{20} coefficients based on GRACE data and an ocean bottom pressure model. Geophys J Int 210(3):1305–1322. https://doi.org/10.1093/gji/ggx241

Swenson S, Wahr J (2006) Post-processing removal of correlated errors in GRACE data. Geophys Res Lett 33:L08402. https://doi.org/10.1029/2005GL025285

Swenson S, Chambers D, Wahr J (2008) Estimating geocenter variations from a combination of GRACE and ocean model output. J Geophys Res Solid Earth 113(8):B08410. https://doi.org/10.1029/2007JB005338

Tapley B, Watkins M, Flechtner F, Reigber C, Bettadpur S, Rodell M, Sasgen I, Famiglietti J, Landerer F, Chambers D, Reager J, Gardner A, Save H, Ivins E, Swenson S, Boening C, Dahle C, Wiese D, Dobslaw H, Tamisiea M, Velicogna I (2019) Contributions of GRACE to understanding climate change. Nat Clim Change 9(5):358–369. https://doi.org/10.1038/s41558-019-0456-2

Tapley BD, Bettadpur S, Watkins M, Reigber C (2004) The gravity recovery and climate experiment: Mission overview and early results. Geophys Res Lett 31:L09607. https://doi.org/10.1029/2004GL019920

Tikhonov AN, Arsenin VY (1977) Solutions of ill-posed problems. V.H.Winston and Sons, Washington

van den Broeke MR, Enderlin EM, Howat IM, Kuipers Munneke P, Noël BP, Jan van de Berg W, van Meijgaard E, Wouters B (2016) On the recent contribution of the Greenland ice sheet to sea level change. Cryosphere 10(5):1933–1946. https://doi.org/10.5194/tc-10-1933-2016

Velicogna I, Wahr J (2013) Time-variable gravity observations of ice sheet mass balance: Precision and limitations of the GRACE satellite data. Geophys Res Lett 40(12):3055–3063. https://doi.org/10.1002/grl.50527

Velicogna I, Mohajerani Y, Geruo A, Landerer F, Mouginot J, Noel B, Rignot E, Sutterley T, van den Broeke M, van Wessem M, Wiese D (2020) Continuity of ice sheet mass loss in Greenland and Antarctica from the GRACE and GRACE Follow-On missions. Geophys Res Lett 47(8). https://doi.org/10.1029/2020GL087291

Wahr J, Molenaar M, Bryan F (1998) Time variability of the Earth's gravity field: Hydrological and oceanic effects and their possible detection using GRACE. J Geophys Res Solid Earth 103(B12):30,205-30,229

Wang L, Burgmann R (2019) Statistical significance of precursory gravity changes before the 2011 M_w 9.0 Tohoku-Oki earthquake. Geophys Res Lett 46:7323–7332. https://doi.org/10.1029/2019GL082682

Wang W, Shen Y, Chen Q, Wang F (2024) High-resolution mascon solutions reveal glacier-scale mass changes over the Greenland Ice Sheet from 2002 to 2022. Geophys J Int 236(1):494–515. https://doi.org/10.1093/gji/ggad439

Wessel P, Smith WHF, Scharroo R, Luis J, Wobbe F (2013) Generic Mapping Tools: Improved version released. Eos Trans AGU 94(45):409–410. https://doi.org/10.1002/2013EO450001

Xu Z, Schrama E, van der Wal W (2015) Optimization of regional constraints for estimating the Greenland mass balance with GRACE level-2 data. Geophys J Int 202(1):381–393. https://doi.org/10.1093/gji/ggv146

Yuan DN (2018) GRACE (Gravity Recovery and Climate Experiment), JPL Level-2 Processing Standards Document (For Level-2 Product Release 06). Jet Propulsion Laboratory, California Institute of Technology